Research Article

Mohamed R. Eid*, Wasim Jamshed, Assmaa Abd-Elmonem, Ahmed F. Al-Hossainy, Nasser Almutlaq, Ayesha Amjad, and Sayed M. El Din

Energy bandgap and thermal characteristics of non-Darcian MHD rotating hybridity nanofluid thin film flow: Nanotechnology application

https://doi.org/10.1515/ntrev-2023-0159
received February 9, 2023; accepted November 3, 2023

Abstract: The primary purpose of this research is to examine how the presence of thermal features variation affects the velocity and heat transfer rate of nanofluids composed of sodium alginate and molybdenum disulfide $[\text{Na-Alg/MoS}_2]^{\text{m}}$ and sodium alginate and molybdenum disulfide and graphene oxide $[\text{Na-Alg/MoS}_2 + \text{GO}]^{\text{h}}$, respectively, flowing between two rotating, permeable plates. Both centripetal and Coriolis forces, which act on a spinning fluid, are taken into account. The impacts of magnetized force, thermal radiative flux, heat source (sinking), and varied pressure in the Darcy–Forccheimer material are considered. Using the physical vapor deposition method, single and hybridity nanofluid thin films of thickness 150 ± 5 nm may be created. The controlling mathematical equations of the suggested model are solved using the Keller-box technique in MATLAB software. The surface friction coefficient of a hybrid nanofluid is less, and the heat transfer rate is greater than that of a regular nanofluid. The rate of heat transmission is slowed by the rotational parameter. The thermal efficiency of mono nanofluids is as low as 6.16% and as high as 21.88% when compared to those of hybrid nanofluids. In particular, the findings of density functional theory (DFT) calculations reveal that the energy bandgap $\Delta E_{\text{g}}^{\text{Opt}}$ drops from 1.641 eV for conventional nanofluid to 0.185 eV for hybridity nanofluid. Based on the findings, the addition of graphene oxide nanoparticles to the base nanofluid converts it from a semi-conductor to a hybridity nanofluid as a superconductor.

Keywords: $[\text{Na-Alg/MoS}_2 + \text{GO}]^{\text{h}}$, rotating flow, structure characteristics, TDDFT, Lorentz force, Keller-box method

*** Corresponding author: Mohamed R. Eid**, Department of Mathematics, Faculty of Science, New Valley University, Al-Kharga, Al-Wadi Al-Gadid, 72511 Egypt; Finance and Insurance Department, College of Business Administration, Northern Border University, Arar 1321, Saudi Arabia, e-mail: m_r_eid@yahoo.com
Wasim Jamshed: Department of Mathematics, Capital University of Science and Technology (CUST), Islamabad, 44000, Pakistan; Mathematics in Applied Sciences and Engineering Research Group, Scientific Research Center, Al-Ayen University, Nasiriyah 64001, Iraq
Assmaa Abd-Elmonem: Department of Mathematics, College of Science, King Khalid University, Abha, Saudi Arabia
Ahmed F. Al-Hossainy: Department of Chemistry, Faculty of Science, New Valley University, Al-Kharga, Al-Wadi Al-Gadid, 72511 Egypt
Nasser Almutlaq: Department of Physics, Faculty of Science, Northern Border University, Arar, 1321, Saudi Arabia
Ayesha Amjad: Faculty of Organization and Management, Silesian University of Technology, Gliwice 44-100, Poland; Centre for Mechanical Engineering, Materials and Processes (CEMMPRE), University of Coimbra, Polo II, Coimbra, 3030-788, Portugal
Sayed M. El Din: Center of Research, Faculty of Engineering, Future University in Egypt, New Cairo, 11835, Egypt

Nomenclature

a	stretching rate
B_0	uniform magnetic field
C_{f}	drag force facto
ϵ	hardness
$E_{\text{g}}^{\text{Opt}}$	energy bandgap
E_{H}	HOMO
E_{L}	LUMO
Er	local inertia
F	coefficient of variable inertia
F', G	nondimensional speeds
K_1	permeability
κ_{f}, κ_{p1}, κ_{p2}	thermal conductivities
m	shape agent
Nu	local Nusselt number
p	pressure
Pr	Prandtl amounts
p_{y}	fluid yield stress
p_1, p_2	solid nanoparticles
q_{w}	surface heat fluxing
S	suction/injection velocity

Open Access. © 2023 the author(s), published by De Gruyter. This work is licensed under the Creative Commons Attribution 4.0 International License.

T	temperature of fluid
T_0	temperature at upwind wall
T_h	temperature at down wall
u, v, w	velocity elements
U_w	stretched surface speed
ν_f	kinematic viscosity
ϑ	softness
λ	porosity
Y	similarity variable
$\sigma_f, \sigma_{p1}, \sigma_{p2}$	electrical conductivities
$\rho_f, \rho_{p1}, \rho_{p2}$	densities
μ_B	plastic dynamic viscosity
Ω	angular velocity
μ_f	dynamic viscosity
χ	electro-negativity
ς	chemical potentiality
ω	electrophilicity-index

Subscripts

f	fluid phase
hbnf	hybrid nanofluid
nf	nanofluid
p_1, p_2	solid nanoparticles

1 Introduction

To bridge the gap between fossil fuels and clean energy systems, renewable energy technologies are now at the forefront of research and development efforts. Due to the fact that solar energy systems are associated with an unlimited energy source, a well-documented theory, simplicity, an environmentally friendly structure, and a noticeably greater energy and exergy efficiency range compared to other renewables, there is no doubt that solar energy systems play the preeminent position among the alternatives. But traditional working fluids with subpar thermophysical qualities are still used in solar energy systems. This is a significant drawback. To put it in another way, more enhancements can still be made to the aforementioned systems by the use of one-of-a-kind nanoparticles (NPs) that possess better thermal, electrical, optical, and mechanical capabilities. Sun thermal collectors that use NPs suspended in a liquid media to scatter and absorb sun energy are referred to as nanofluid-based direct solar collectors.

Nanofluids are solid–liquid composites made up of nanometer-sized solid molecules, fibers, rods, or tubes floating in various basic liquids, providing interesting technical possibilities for improving heat transmission despite its numerous benefits while causing peculiar thermal variations. The reproduction of nanofluids is mentioned in the evolutionary theory of adding solid particles to heat transfer fluids to increase thermal flexibility. This new idea was introduced by Maxwell in 1873. Because of the size impact and Brownian dispersion of NPs in fluids, nanofluids have more stability than normal liquids augmented with solid particles of micrometer or millimeter size. Nanofluids may operate easily in the microchannel heat sink without clogging with such ultra-fine nanomaterials, and the size of the heat transmission system can be lowered to employ nanofluids for effective heat transfer efficiency [1]. Nanofluids offer several advantages owing to their heat transfer stiffness and dispersion resilience. A significant quantity of space increases heat transmission between liquids and particulates [2]. The single-step technique is a practice that requires the manufacture of NPs as well as the fabrication of nanofluids, in which the nanomaterials are generated immediately using the physical vapor deposition (PVD) technique or the liquid chemical approach. As a result of avoiding the drying, storage, distribution, and dispersion of nanomolecules, the fusing of nanomolecules is minimized, and the liquid's permanence is enhanced. The disadvantage of this strategy is that only the low-pressure vapor fluid is compatible with the procedure. This decreases the technique's usage [3]. The method of electrospinning into basic liquids is a two-step procedure for producing nanoliquids. The nanomaterials, nanowires, or nanotubes utilized in this procedure are first created as a dry powder by evaporation gas, chemical evaporation, mechanical metal alloys, or other appropriate processes, and then dissolved in a liquid in the second stage. This method divides the preparation of nanofluids from the preparation of NPs. As a result, nanoscale agglomerates may happen at both phases, notably during the setup, storage, and transportation of the nanoscale. Aggregation not only causes micro-channels to break down and close but it also reduces heat conductance. To minimize particle bonding and increase the activities of different liquids, simple approaches such as supersonic combining or the inclusion of surfactants in liquids are frequently utilized. Because numerous businesses have indeed advanced nanopowder synthesis processes for industrial production levels, there may be cost benefits in adopting two strategies that rely on the usage of such powders. However, one critical issue that must be addressed is the robustness of the prepared suspension [4,5]. Peng *et al.* [4] investigated the parameters that determine nanofluid stability. The experimental findings revealed that the most critical elements influencing suspended stabilization were NPs concentricity, dispersion, liquid base viscidness, and pH value. The diversity, scope, NPs density, and

ultrasonic vibration of nanofluids all contribute to their stability. Hwang *et al.* [6] used a UV-vis spectrophotometer to investigate the stability of nanoliquid. He felt that the features of fixed particulates and basic liquids, such as morphological particles, compositions of molecules, and basic liquids, had a significant impact on the stability of nanofluids. Furthermore, the inclusion of surfactant can increase the stabilization of the solution. Wang [7] also believes that the nanomolecules' identical diameter and the varied viscidness of the nanoliquids are the most critical elements influencing the stability of the NPs suspension. The authors also found that the right pH value of nanofluids, as well as a high percentage of surfactants, had a substantial influence on nanofluid stabilization.

Hybrid NPs are described as NPs composed of two or more diverse nano-meter dimensions. The liquid arranged by compound NPs is identified as hybrid nanofluid (HNF). A recent review of the nanofluid layer, the hybrid nanofluid, which combines complex particles with a complex composite of many NPs, aims to correct the degradation of mono nanofluid compounds by synthesizing any damage to mono nanofluid [8]. Hybrid nanoliquids work very well in terms of cooling when temperatures are high and cover a wide range of thermal materials. HNFs are usually prepared by dissolving two different types of NPs in basic liquids and are emerging as new nanotechnology [9]. HNF gains a higher rate of heat transfer compared to pure liquid as evidenced by experiments and numbers by many scientists. Choi [10]. were the earliest to apply a nanofluid that improved heat transmission rate compared to normal liquid. In 1995, she revealed her results at the Argonne National Laboratory. At the time, nanofluid was thought to be the next generation of heat transmission fluid because it offered exhilarating prospects to increase thermal efficiency above standard liquid [11]. This study has opened a new method for engineering systems due to the beneficial effects of manipulating nanofluids. Numerous tests have been performed and two categories of molecules have been suspended in basic fluids, namely "Hybrid nanofluid". In the examination of Sidik *et al.* [11] HNF increases the heat transfer rate compared to nanofluid and light liquid. A mixture of multiwall sphere-shaped silica nanotubes mixture nanostructures and a thermal performance study of the corresponding nanofluid was probed by Choi and Eastman [12]. HNFs are very effective in terms of cooling when temperatures are high and include many thermal systems. HNFs are usually prepared by dissolving two different types of NPs in basic liquid and are emerging as new nanotechnology. Different types of synthetic nanofluids were prepared and studied by previous researchers under the requirements essential for their studies. Based on literature reviews, the HNF exhibits greater thermal transfer and rheological properties compared to the base fluid and mono nanofluid [13].

Non-Newtonian nanofluids are complex due to the indirect relationship between stress and stress rate, and this is because many phenomena in the real world are non-linear and are often described in non-linear expressions. A line problem is simple to answer but finding solutions to indirect difficulties is more challenging. Despite the availability of increasingly efficient processors, finding a clear exact solution to a given indirect issue is sometimes more difficult than obtaining a cost-effective solution [14]. However, when the findings of numerical approaches are sorted otherwise, they produce unstable spots; acquiring a thorough knowledge of the indirect issue is also challenging. If an indirect problem includes unity or has several solutions, the numbers get more complicated. While computational and mathematical approaches for handling indirect issues have limitations, they do offer benefits. As a result, we cannot dismiss any of these techniques, yet it is typically enjoyable to address an indirect issue through research [15]. Casson liquid is categorized as a non-Newtonian liquid and results in its rheologic properties related to shearing stress–strain relationships. It acts as elasticity in the lower shear strain and in addition to the critical amount of stress it behaves like a Newtonian liquid. Mustafa *et al.* [16] used a solution for homotopy analysis to investigate the flowing of this type of liquid boundary near the vertical position and presented the results of a limited case where the Casson factor manages to be infinite. Wang *et al.* [17] studied the development and formation of a hot boundary layer in Casson liquid motion over a solid surface in which both the surrounding liquid and the flat plate were maintained simultaneously and the heating of the flat plate abruptly surged in that surrounding liquid. They discovered parabolic partial variations that were resolved using the homotopy analysis approach. Makanda *et al.* [18] examined the 2-dimensional flowing and distribution of a specific type of chemical in the Casson fluid from an unstable expandable area where there is a magnetic field. It has often been observed that increasing magnetic and input parameters reduces velocity profiles, heat transmission coefficient, and concentricity outlines while drag tension increases. Hayat *et al.* [19] presented the Soret and Dufour effects on the two-dimensional flow of Casson fluid created by an expandable electric field. They used a homotopy analysis method to solve an incorrect system of different standardized calculations. Mukhopadhyay [20] investigated the consequences of thermal radiative on Casson liquid flowing and heat transference to a non-volatile stretchy region under absorbance/pulse and found that the Prandtl quantity may be employed to boost the cooling rate in Casson liquid flowing and temperature. An

increment in the radiative parameter reinforces the profile, while the Casson variable decreases the boundary density and boosts the temperature boundary layer thickening. Rajan *et al.* [21] investigated the thermal characteristics and the flowing of Casson fluid via a stretchable surface in the existence of thermal radiative fluxing, magnetized force, viscous dissipative, heat generating, and chemical reactions influences. They discovered that the swelling heat generating factor decreased the temperature outlines in the boundary layer. Casson nanofluid unstable flowing has received little attention so far.

Magnetohydrodynamics (MHD) describes the extreme behavior of electromagnetic liquids in a magnetic field. MHD estimates that the electric field disappears into the moving water frame, without the potential effects of resistance [22]. MHD is about the interaction between moving fluids and the magnetism force. Ionization of the gas occurs at a rate that changes with increasing temperature due to the effective magnetic force that is created by the electrical force of the flow of this gas around a metal rod. Many fields in industry, engineering, and technology may benefit from models based on nanofluids and their behavior, such as those using heating or cooling systems. There has been a lot of research on MHD convection flowing of nanoliquids during the last decade. Two types of models have been used for the nanofluid flow, one-phase and two-phase approaches. In the two-phase approach, the basic fluid is considered a continuous phase, and the fixed particles are considered a continuous/clear phase, and the old Euler and Euler-Lagrange procedures are employed to mimic the flow [24]. Joule heating is a physical impact when the transfer of electrical energy to an electric electrode produces thermal energy. This thermal energy is demonstrated by the increase in the temperature of the conductor, hence the term "heat." Joule heating is the process by which electrical energy is converted into thermal energy, in accordance with the principle of energy conservation [25]. Over the past few years, synthetic nanofluids have emerged as extensions of nanofluids and are believed to enhance their thermophysical and rheological properties and heat transfer properties. HNF was developed by combining basic liquids with a mixture of a composite type of distinctly formed NPs [26].

A source of heating system where heat is lost to the heat sink for example, in a built environment, a radiator may be considered a source of heat, while the surrounding space, which heats up through the process of radiation and convection, may be considered a hot spot [27]. Some items may serve as unintentional heat sources, which may not be desirable as they may cause excessive heat, such as people, computers, ovens, and other appliances. These heat sources are sometimes called heat loads. Heat sinks may include air conditioning systems, refrigeration equipment, heat weight, *etc*. A heat sink, in the context of thermodynamics, refers to a heat reservoir that has the ability to absorb a limitless quantity of heat while experiencing little changes in temperature. To facilitate the transmission of heat by convection, radiation, and conduction, heat sinks for electronics equipment need to maintain a temperature that is higher than the ambient environment. Due to the inherent inefficiency of power supply in electronics, excess heat is generated, which may have a negative impact on the device's performance. Consequently, the construction incorporates a heat sinking to dissipate heat [28]. The temperature change will usually be accompanied by an increase in the pressure of the hole. If the soil is compacted enough these hole pressures will disappear. This study develops an analytical solution to the basic problem of the point heat source buried deep in the ground [29].

The applications that are most common for molybdenum disulfide NPs are in the realm of lubricants and greases. Examples of technology that are difficult to maintain include space vehicles and satellites, as well as some military fields. When utilized molybdenum disulfide NPs as an item in these composites. Mechanical exfoliation may be seen in things like photodetectors, optoelectronic devices, and sensors, among other things. In the case of liquid exfoliation, some examples include quantum dots, nanoplatelets, and energy storage devices. MoS_2 does not need surface treatments to avoid strong interactions with biomolecules, which opens a greater voltage range. This is one of the benefits of using this material. In this way, MoS_2 is used in biomedical technological endeavors such as single-molecule sequencing of DNA. Graphene oxide (GO), a graphene product that has been oxygenated is now being used in the fields of biotechnology and medical procedures for the treatment of cancer, the transport of drugs, and cellular visual storytelling. Utilizing decreased GO may be beneficial for a variety of applications, including those involving technological devices, storage of energy, (bio) sensors, applications in healthcare, tissues, catalysts, supercapacitors, and procedures for purifying water.

The purpose of this research is to integrate theoretical and experimental evaluations of the flow and thermal transmission analyses of Casson nanofluids (*i.e.*, sodium alginate and molybdenum disulfide $[Na\text{-}Alg/MoS_2]^m$ and sodium alginate and molybdenum disulfide and graphene oxide $[Na\text{-}Alg/MoS_2 + GO]^h$) within solar aircraft wings as two parallel sheets in a parabolic trough solar collector (PTSC). Different factors, such as heat production, flow rate, and thermal radiation, were included in an analysis of wings' heat transfer ability. The kinetic and energy

control formulae have been examined using the Keller-box method (KBM), a well-established numerical technique. We quickly examine and display in charts and tables how different variables affect the velocity, shear stress, and temperature fields, as well as the surface frictional factor and Nusselt number. Notably, $[Na\text{-}Alg/MoS_2]^m$ and $[Na\text{-}Alg/MoS_2 + GO]^h$ with a thickness of 150 ± 5 nm are fabricated using the PVD technology. The LUMO model, HOMO, and FTIR were used to analyze thin films that were created using DMOl^3/TDDFT-DFT for both the $[Na\text{-}Alg/MoS_2]^m$ and $[Na\text{-}Alg/MoS_2 + GO]^h$ combinations. A schematic of the investigated flow model is shown in Figure 1.

2 Experimental work

2.1 Materials and methods

The molecular formula list and chemical suppliers utilized in previous studies are stated in Table 1. Utilization of all chemicals was done after obtaining them without further processing. Also, the list of techniques regarding characterization as well as standard conditions are given Table 1.

2.2 Synthesis of $[MoS_2]^{NPs}$ using sol–gel method

MoS_2 aerogel NPs produced using the polymerized sol–gel process are presented in Figure 2 as a flow chart [30].

2.3 Synthesis of $[Na\text{-}Alg/MoS_2]^m$ and $[Na\text{-}Alg/MoS_2 + GO]^h$

In closed glass-flask to avoid the hydrolysis effect due to the humidity, $[MoS_2]^{NPs}$ as well as [Na-Alg + C_2H_5OH]/298 K, $[MoS_2]^{NPs}$ mixed together with [Na-Alg + C_2H_5OH] by the usage of a magnetic stirrer. C_2H_5OH/99% solution was added to a solid combination of $[MoS_2]^{NPs}$ and [Na-Alg + C_2H_5OH] for the preparation of homogeneous $[Na\text{-}Alg/MoS_2]^m$. Production of modeled white precipitates was done under an aggregation state which was for 30 min. The centrifuge was employed for the extraction of acquired participants after aggregation. Pure C_2H_5OH was utilized for the removal of unreacted parts from base liquid (Na-Alg) [31]. HNFs that were formed by the reaction of $[GO]^{NPs}$ with $[Na\text{-}Alg/MoS_2]^m$ produced $[Na\text{-}Alg/MoS_2 + GO]^h$ at optimum conditions.

2.4 Fabrication of $[Na\text{-}Alg/MoS_2]^m$ and $[Na\text{-}Alg/MoS_2 + GO]^h$ thin films

$[Na\text{-}Alg/MoS_2]^m$ and $[Na\text{-}Alg/MoS_2 + GO]^h$ powder at 25°C were mixed in a solution of C_2H_5OH/99 %. Various weights (20, 30, 40, and 50 mg) of $[Na\text{-}Alg/MoS_2]^m$ and $[Na\text{-}Alg/MoS_2 + GO]^h$ were dissolved in 5 mL of C_2H_5OH solution. Thin films of $[Na\text{-}Alg/MoS_2]^m$ and $[Na\text{-}Alg/MoS_2 + GO]^h$ (Figure 3) were deposited on quartz substrate utilizing the PVD method using a UNIVEX 250 Leybold (Cologne, Germany). Multiple instruments for measuring thin-film thickness ≅ 150 ± 5 nm here in UNIVEX units are available. The decision is dependent

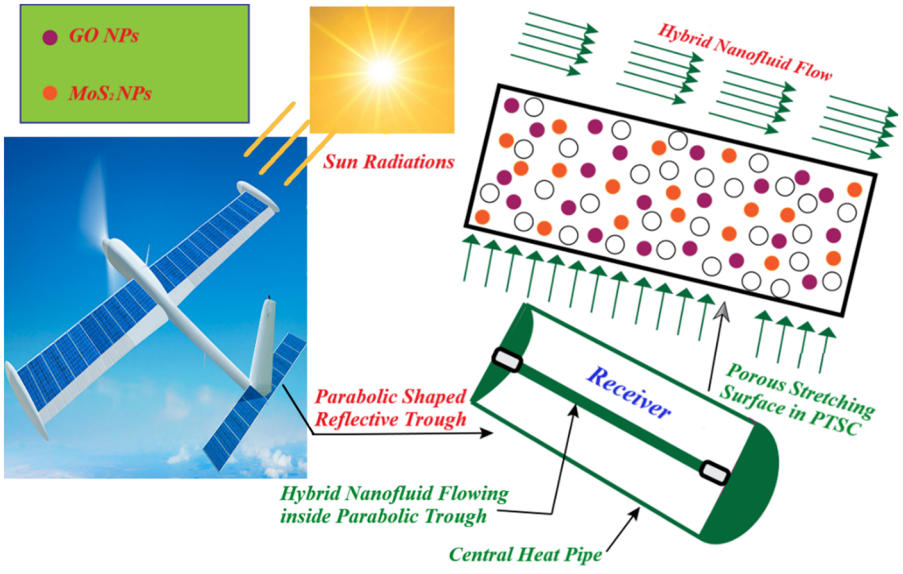

Figure 1: Schematic of flow model.

Table 1: List of materials and methods

Material			Methods	
Reagent	**M formula**	**Supplier**	**Apparatus**	**Models and specifications**
Sodium alginate	$C_6H_9NaO_7$	Sigma & Aldrich	Ultrasonic cleaner	SB-420DDT
Molybdenum trioxide	MoO_3	Sigma & Aldrich	Ionized H_2O	IONIA alkaline generator electrolysis apparatus JP-107
Ammonium persulfate	$(NH_4)_2S_2O_8$	Merck	FTIR Spectra	Perkin-Elmer FT-IR type 1650
Citric acid	$C_6H_8O_7$	Merck Millipore	PVD technique	UNIVEX 250 Leybold (Cologne, Germany)
Ethylene glycol	$C_2H_6O_2$	Aldrich	p-Si	p-type (single crystal)
Dimethyl formaldehyde	C_3H_7NO	Sigma & Aldrich		

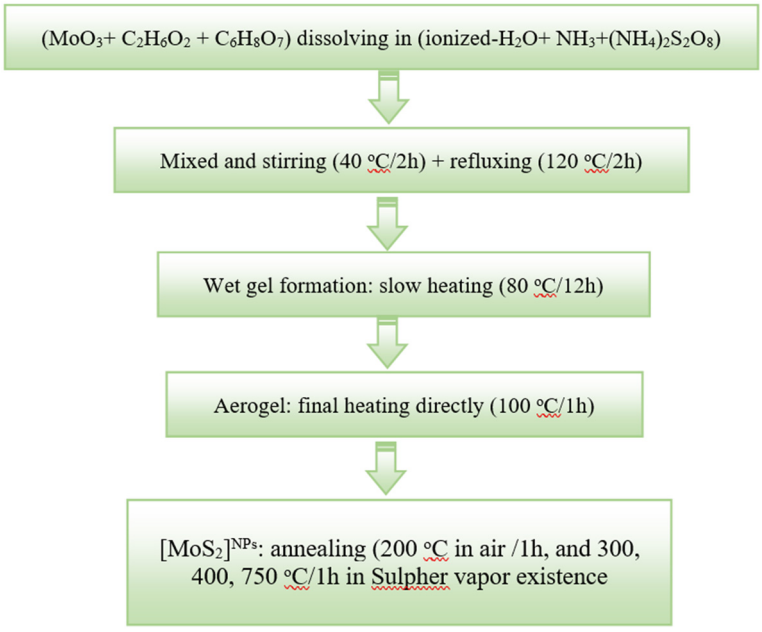

Figure 2: Flow chart of the preparation process of $[MoS2]^{NPs}$ using the sol–gel method.

on appropriate evaluations and automation. The usage of crystal systems that oscillate is the norm. This may have one or more sensor heads, and it is designed for use in ultra-high-vacuum environments [32].

2.5 Computational analysis

The results of the $DMol^3$ computation is generated from the frequency analyses as well as performance-related molecular structure regarding $[Na\text{-}Alg/MoS_2]^m$ and $[Na\text{-}Alg/MoS_2 + GO]^h$ in the density functional theory (DFT) in gas phases state. $DMol^3$ was used in order to investigate the approximated indicators of PBE/GGA functioning, natural pseudo-positive preservation agents, and also a simple DNP set for approved chemicals [33]. According to the results of the computations carried out by a computer, the total amount of plane-wave power cut-off was 830 eV. Using $DMol^3$ IR features, for instance, spectroscopic and physical properties of $[Na\text{-}Alg/MoS_2]^m$ and $[Na\text{-}Alg/MoS_2 + GO]^h$ were found, which led to a GP frequency estimate.

In addition, the operation of Becke [34] and Lee *et al.* (B3LYP) [35] with WBX97XD/6-311G may be modified by three factors, which have been determined to be the shape and vibrant regularity (IR), $[Na\text{-}Alg/MoS_2]^m$, and $[Na\text{-}Alg/MoS_2 + GO]^h$ in the gas phase, along with nanofluid in the gaseous phase. These variables have increased. The computer program of the GAUSSIAN 09W system investigates symmetric variations, pictures of enhancements, power, and vibration concerning nanocomposite mixes that have been treated. The WBX97XD/6-311G B3LYP technique has produced various valuable pieces of details on the relationship between the setting and the variety of outcomes that our group has supplied [36]. The GAUSSIAN 09W and $DMOl^3$

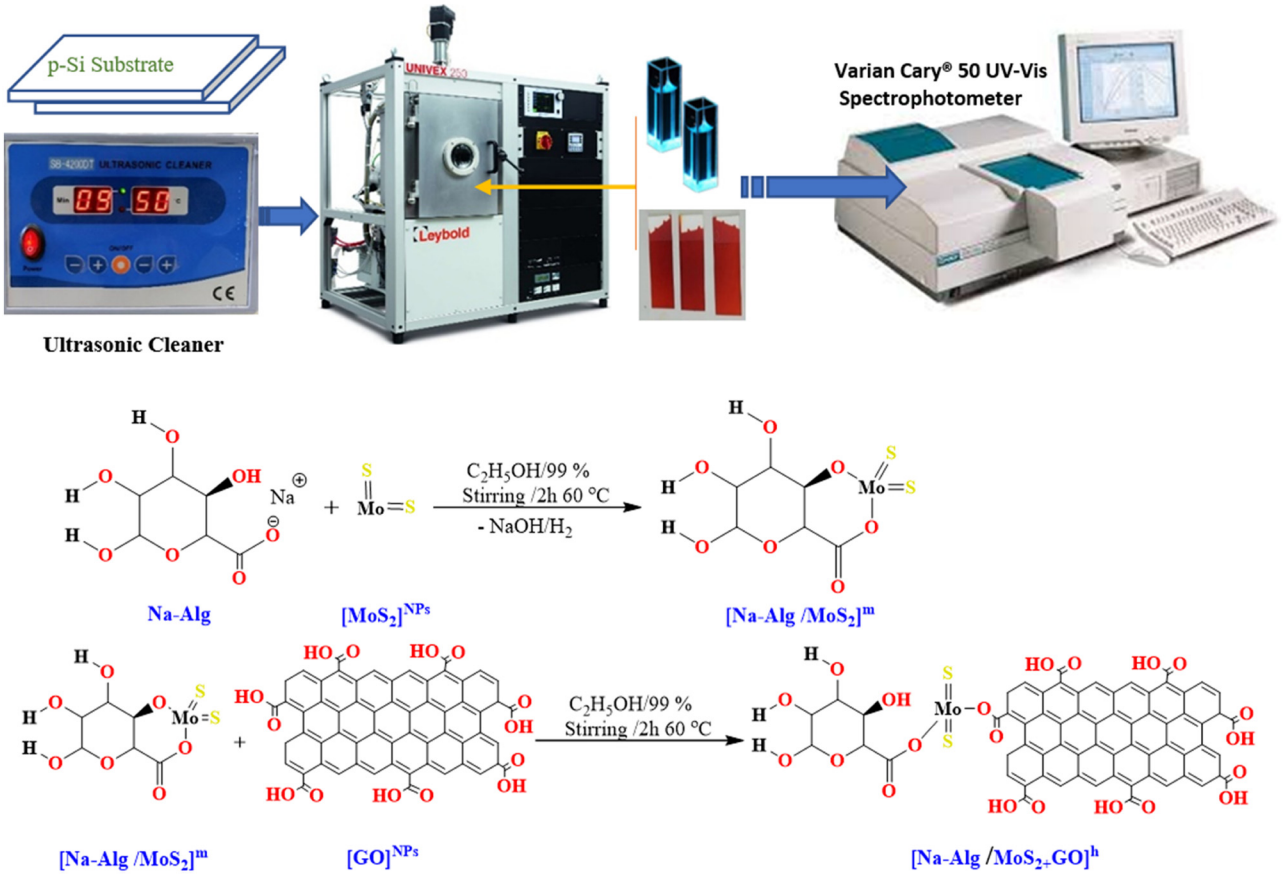

Figure 3: Fabrication process of thin films of nanofluids together with a technique for [Na-Alg/MoS_2]^m and [Na-Alg/MoS_2 + GO]^h.

approaches are used to evaluate the representations of [Na Alg/MoS_2]^m and [Na-Alg/MoS_2 + GO]^h in isolated molecules, intentional adjustments in descriptors, prototype vitality data, and the utilization of various modifications with a variety of challenges.

3 Mathematical modeling

A 3-dimensional, time-independent, MHD, and revolving flow of ([Na-Alg/MoS_2 + GO]^h) hybrid nanomaterial lying among two plates with angular velocity Ω $[0, \Omega, 0]$ in the effect of heat transference has been examined in the present analysis. $U_w = ax(a > 0)$ represents the stretched velocity regarding the lower plate while the upper surface is permeable. $V = [u, v, w]$ is the flow field velocity. There is a constant magnetic field B_0 in the direction of y-axis. At low magnetism Reynolds quantity assumption, induced magnetism force is ignored. The physical flow model as well as the related coordinate system is specified in Figure 4. The constitutive model specifying Casson fluid is as follows [18]:

$$\tau_{ij} = \begin{cases} \left(2\mu_B + \dfrac{\sqrt{2}p_y}{\sqrt{\pi}}\right)e_{ij} & \text{if} \quad \pi > \pi_c \\ \left(2\mu_B + \dfrac{\sqrt{2}p_y}{\sqrt{\pi_c}}\right)e_{ij} & \text{if} \quad \pi < \pi_c, \end{cases} \tag{1}$$

where μ_B is the dynamical viscidness of liquid, p_y is the yield stress, e_{ij} is the deformation rate component, and $\pi = e_{ij}e_{ij}$.

Following is a component form of governing PDEs [18,37]:

$$u_x + v_y = 0, \tag{2}$$

$$\rho_{hbnf}(uu_x + vu_y + 2\Omega w) = -p_x^{**} + \left(1 + \frac{1}{\beta}\right)\mu_{hbnf}(u_{xx} + u_{yy}) - \frac{\nu_{hnf}}{K_1}u - Fu^2 - \sigma_{hbnf}B_0^2 u, \tag{3}$$

$$\rho_{hbnf}(uv_x + vv_y) = -p_y^{**} + \left(1 + \frac{1}{\beta}\right)\mu_{hbnf}(v_{xx} + v_{yy}), \tag{4}$$

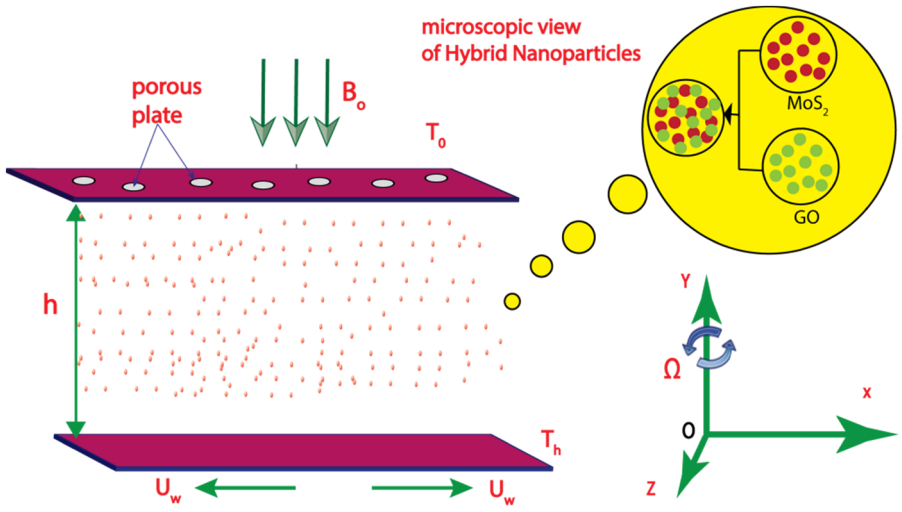

Figure 4: Geometry of the problem.

$$\rho_{\text{hbnf}}(uw_x + vw_y - 2\Omega u) = \left(1 + \frac{1}{\beta}\right)\mu_{\text{hbnf}}(w_{xx} + w_{yy}) - \frac{\nu_{\text{hnf}}}{K_1}w - Fw^2 - \sigma_{\text{hbnf}}B_0^2 w, \tag{5}$$

$$uT_x + vT_y = \alpha_{\text{hbnf}}(T_{xx} + T_{yy}) + \frac{1}{(\rho C_{\text{p}})_{\text{hbnf}}}\frac{16\sigma^* T_\infty^3}{3\kappa^*}T_{yy} + \frac{Q_0(T - T_0)}{(\rho C_{\text{p}})_{\text{f}}}, \tag{6}$$

where $\alpha_{\text{hbnf}} = \frac{\kappa_{\text{hbnf}}}{(\rho C_{\text{p}})_{\text{hbnf}}}$ is the thermal diffusion of HNF while $p^{**} = p - \frac{\Omega^2 x^2}{2}$ is the varied pressure.

For [Na-Alg/MoS_2]$^{\text{m}}$ and [Na-Alg/MoS_2+GO]$^{\text{h}}$, the expressions are given in Tables 2 and 3. Thermal gradient is formulated on HNF. Temperature of the upper wall is T_0 while that of the lower wall is T_{h} with $T_0 < T_{\text{h}}$. Thermo-physical features of MoS_2, Na-Alg, as well as GO, are given in Table 4.

The endpoint constraints at the upstair and downstair walls are as [37] follows:

$$\left.\begin{aligned} &\text{at} \quad y = 0, u = U_{\text{w}} = ax, v = w = 0, T = T_{\text{h}}, \\ &\text{at} \quad y = h, u = 0, v = -W_0, w = 0, T = T_0. \end{aligned}\right\} \tag{7}$$

Table 2: Thermophysical properties of nanofluid [38]

Properties	Nanofluid
μ	$\mu_{\text{nf}} = \frac{\mu_{\text{f}}}{(1-\phi)^{2.5}}$
ρ	$\rho_{\text{nf}} = (1-\phi)\rho_{\text{f}} + \phi\rho_{\text{p}}$
(ρC_{p})	$(\rho C_{\text{p}})_{\text{nf}} = (1-\phi)(\rho C_{\text{p}})_{\text{f}} + \phi(\rho C_{\text{p}})_{\text{p}}$
κ	$\frac{\kappa_{\text{nf}}}{\kappa_{\text{f}}} = \frac{(\kappa_{\text{p}} + (m-1)\kappa_{\text{f}}) - (m-1)\phi(\kappa_{\text{f}} - \kappa_{\text{p}})}{(\kappa_{\text{p}} + (m-1)\kappa_{\text{f}}) + \phi(\kappa_{\text{f}} - \kappa_{\text{p}})}$
σ	$\frac{\sigma_{\text{nf}}}{\sigma_{\text{f}}} = 1 + \frac{3(\sigma_{\text{s}} - \sigma_{\text{f}})\phi}{(\sigma_{\text{s}} + 2\sigma_{\text{f}}) - (\sigma_{\text{s}} - \sigma_{\text{f}})\phi}$

Table 3: Thermo physical aspects of HNF [38]

Properties	HNF
μ	$\Psi_1 = \frac{\mu_{\text{hbnf}}}{\mu_{\text{f}}} = ((1-\phi_{\text{a}})^{2.5})^{-1}((1-\phi_{\text{b}})^{2.5})^{-1}$
ρ	$\Psi_2 = \frac{\rho_{\text{hbnf}}}{\rho_{\text{f}}} = (1-\phi_{\text{b}})\{(1-\phi_{\text{a}}) + \phi_{\text{a}}\frac{\rho_{\text{p}_1}}{\rho_{\text{f}}}\} + \phi_{\text{b}}\frac{\rho_{\text{p}_2}}{\rho_{\text{f}}}$
(ρC_{p})	$\Psi_3 = \frac{(\rho C_{\text{p}})_{\text{hbnf}}}{(\rho C_{\text{p}})_{\text{f}}} = (1-\phi_{\text{b}})\{(1-\phi_{\text{a}}) + \phi_{\text{a}}\frac{(\rho C_{\text{p}})_{\text{p}_1}}{(\rho C_{\text{p}})_{\text{f}}}\} + \phi_{\text{b}}\frac{(\rho C_{\text{p}})_{\text{p}_2}}{(\rho C_{\text{p}})_{\text{f}}}$
κ	$\Psi_4 = \frac{\kappa_{\text{hbnf}}}{\kappa_{\text{f}}} = \left[\frac{(\kappa_{\text{p}_2} + (m-1)\kappa_{\text{nf}}) - (m-1)\phi_{\text{b}}(\kappa_{\text{nf}} - \kappa_{\text{p}_2})}{(\kappa_{\text{p}_2} + (m-1)\kappa_{\text{nf}}) + \phi_{\text{b}}(\kappa_{\text{nf}} - \kappa_{\text{p}_2})}\right] \times \left[\frac{(\kappa_{\text{p}_1} + (m-1)\kappa_{\text{f}}) + \phi_{\text{a}}(\kappa_{\text{f}} - \kappa_{\text{p}_1})}{(\kappa_{\text{p}_1} + (m-1)\kappa_{\text{f}}) - (m-1)\phi_{\text{a}}(\kappa_{\text{f}} - \kappa_{\text{p}_1})}\right]$
σ	$\Psi_5 = \frac{\sigma_{\text{hbnf}}}{\sigma_{\text{f}}} = \left[1 + \frac{3\left(\frac{(\phi_{\text{a}}\sigma_{\text{p}_1} + \phi_{\text{b}}\sigma_{\text{p}_2})}{\sigma_{\text{f}}} - (\phi_{\text{a}} + \phi_{\text{b}})\right)}{\left(\frac{(\phi_{\text{a}}\sigma_{\text{p}_1} + \phi_{\text{b}}\sigma_{\text{p}_2})}{(\phi_{\text{a}} + \phi_{\text{b}})\sigma_{\text{f}}} + 2\right) - \left(\frac{\phi_{\text{a}}\sigma_{\text{p}_1} + \phi_{\text{b}}\sigma_{\text{p}_2}}{\sigma_{\text{f}}} - (\phi_{\text{a}} + \phi_{\text{b}})\right)}\right]$

Similarity transformations are [18] as follows:

$$u = axF'(Y), v = -ahF(Y), w = axG(Y), \quad \theta(Y) = \frac{T - T_0}{T_h - T_0}, \quad Y = \frac{y}{h}. \tag{8}$$

The resulting dimensionless system of ODEs is provided by

$$\left(1 + \frac{1}{\beta}\right)F^{iv} - B_1\Psi_1\Psi_2(F'F''' - FF''') - 2B_2\Psi_1\Psi_2G' - B_1B_3\Psi_1\Psi_5F'' - \Psi_2\gamma F' - 2\Psi_2E_rF'F'' = 0, \tag{9}$$

$$\left(1 + \frac{1}{\beta}\right)G'' - B_1\Psi_1\Psi_2(GF' - FG') + 2B_2\Psi_1\Psi_2F' - B_1B_3\Psi_1\Psi_5G - \Psi_2\gamma G - 2\Psi_2E_rG^2 = 0, \tag{10}$$

$$\left(1 + \frac{4}{3N_r\Psi_4}\right)\theta'' + \Pr B_1\frac{\Psi_3}{\Psi_4}F\theta' - \Pr\delta\Psi_3\theta = 0, \tag{11}$$

having subsequent nondimensional endpoint constraints as follows:

$$\left.\begin{aligned} &F(0) = 0, \quad F'(0) = 1, G(0) = 0, \theta(0) = 1, \\ &F(1) = S, G(1) = 0, \quad F'(1) = 0, \theta(1) = 0. \end{aligned}\right\} \tag{12}$$

Linkage between dimensionless parameters and nondimensional equations are as follows:

$$\left.\begin{aligned} B_1 &= \frac{ah^2}{\nu_f} \text{ (Reynolds number)}, \\ B_2 &= \frac{\Omega h^2}{\nu_f} \text{ (rotation parameter)}, \\ B_3 &= \sqrt{\frac{\sigma_f}{\rho_f a}B_0^2} \text{ (Hartmann number)}, \\ N_r &= \frac{\kappa^*\kappa_f}{4\sigma^*T_\infty^3} \text{ (radiation parameter)}, \\ \delta &= \frac{Q_0}{a(\rho C_p)_f} \text{ (heat generation /absorption coefficient)}, \\ \gamma &= \frac{h^2\nu_f}{aB_0} \text{ (porosity parameter)}, \\ E_r &= \frac{h^2C_b(B_0)^{-0.5}}{\rho} \text{ (local inertia)}, \\ \Pr &= \frac{\mu_f(C_p)_f}{\kappa_f} \text{ (Prandtl number)}. \end{aligned}\right\} \tag{13}$$

The dimensional form of local Nusselt number Nu_x as well as the skin-friction coefficient C_f is described below [32,38].

$$C_f = \frac{2\tau_w}{\rho_{hbnf}U_w^2}, \mathrm{Nu}_x = \frac{xq_w}{k_{hbnf}(T_w - T_\infty)}, \tag{14}$$

Table 4: Thermo-physical characteristics of regular liquid and NPs

Physical properties	Na-Alg	MoS_2	GO
ρ (kg/m^3)	989	5.06×10^3	1,800
C_p (J/kg K)	4,175	397.21	717
κ (W/m K)	0.6376	904.4	5,000
σ (Ω m)$^{-1}$	2.6×10^{-4}	2.09×10^{-4}	1.1×10^{-5}
Pr	13.09	—	—

where $\tau_w = \mu_{hbnf}\left(1 + \frac{1}{\beta}\right)u_y$ is the shearing stress and $q_w = -k_{hbnf}T_y$ is the wall heat fluxing. Nondimensional form of equation (14) *via* similarity alterations of equation (8) is observed as follows:

$$\left.\begin{aligned} C_f\mathrm{Re}_x^{1/2} &= \frac{\Psi_2}{\Psi_1}\left(1 + \frac{1}{\beta}\right)F''(0), \quad \mathrm{Re}_x^{-1/2}\mathrm{Nu}_x = -\theta'(0), \\ C_f\mathrm{Re}_x^{1/2} &= \frac{\Psi_2}{\Psi_1}\left(1 + \frac{1}{\beta}\right)F''(1), \quad \mathrm{Re}_x^{-1/2}\mathrm{Nu}_x = -\theta'(1), \end{aligned}\right\} \tag{15}$$

where $\mathrm{Re}_x = \frac{U_x}{\nu_f}$ represents the local Reynolds number.

4 Numerical implementations

For many values of factors, the Keller-box method scheme [39,40] using the algebraic program MATLAB is employed to resolve the non-linear system of Eqs. (9)–(11) and concerns the endpoint constraint (12). The KBM chart is represented by a flowing map (Figure 5).

4.1 Conversion of ODEs

In order to convert higher order ODEs into first-order ODEs, many substitutions have been introduced. Following are dependent variables Zr_1, Zr_2, Zr_3, Zr_4, Zr_5, Zr_6, Zr_7, and Zr_8 such that

$$\mathrm{Zr}_1 = F, \mathrm{Zr}_2 = F', \mathrm{Zr}_3 = F'', \mathrm{Zr}_4 = F''', \mathrm{Zr}_5 = G, \mathrm{Zr}_6 = G', \mathrm{Zr}_7 = \theta, \mathrm{Zr}_8 = \theta'. \tag{16}$$

$$\frac{d\mathrm{Zr}_1}{dY} = \mathrm{Zr}_2, \tag{17}$$

$$\frac{d\mathrm{Zr}_2}{dY} = \mathrm{Zr}_3, \tag{18}$$

$$\frac{d\mathrm{Zr}_3}{dY} = \mathrm{Zr}_4, \tag{19}$$

$$\frac{dZr_5}{dY} = Zr_6, \tag{20}$$

$$\frac{Zr_7}{dY} = Zr_8, \tag{21}$$

$$\left(1 + \frac{1}{\beta}\right)\frac{dZr_4}{dY} - \Psi_1\Psi_2B_1Zr_2Zr_3 + \Psi_1\Psi_2B_1Zr_1Zr_4 - 2B_2\Psi_1\Psi_2Zr_6 - \Psi_1\Psi_5B_1B_3Zr_3 - \Psi_2\gamma Zr_2 - 2\Psi_2ErZr_2Zr_3 = 0, \tag{22}$$

$$\left(1 + \frac{1}{\beta}\right)\frac{dZr_6}{dY} - \Psi_1\Psi_2B_1Zr_2Zr_5 + \Psi_1\Psi_2B_1Zr_1Zr_6 + 2B_2\Psi_1\Psi_2Zr_2 - \Psi_1Y_5B_1B_3Zr_5 - \Psi_2\gamma Zr_5 - 2\Psi_2ErZr_5^2 = 0, \tag{23}$$

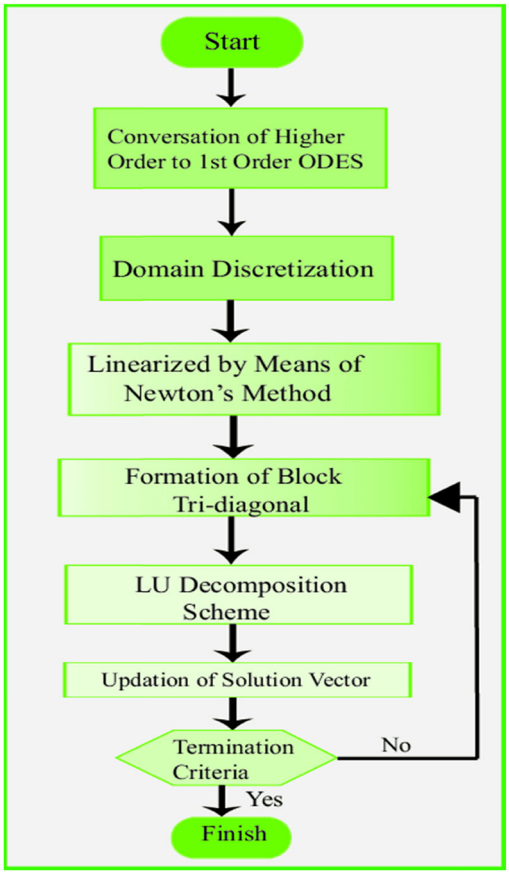

Figure 5: Flowing map explaining KBM.

$$\left(1 + \frac{4}{3N_r\Psi_4}\right)\frac{dZr_8}{dY} + \Pr D_1\frac{\Psi_3}{\Psi_4}Zr_1Zr_8 - \Pr\delta\Psi_3Zr_7 = 0, \tag{24}$$

$$\left.\begin{aligned} Zr_1(0) = 0, \quad Zr_2(0) = 1, \quad Zr_5(0) = 0, \quad Zr_7(0) = 1, \\ Zr_1(1) = 0, \quad Zr_2(1) = 0, \quad Zr_5(1) = 0, \quad Zr_7(1) = 0. \end{aligned}\right\} \tag{25}$$

5 Code validity

To determine the precision of providing KBM solution, the comparison is made between some of our findings and those of Hussain *et al.* [41] for $-\theta'(0)$ in the condition of varied values of sucking parameter S with other factors held fixed. Obtained outcomes are extremely accurate as well as authentic, demonstrating that the present numerical technique is quite trustworthy because of numerical calculation (Table 5).

6 Outcomes and review

The fluidity and thermal transferring ability of an interesting concoction of molybdenum disulfide with sodium alginate ($[\text{Na-Alg/MoS}_2]^m$ along with HNF combined with GO as $[\text{Na-Alg/MoS}_2 + \text{GO}]^h$ have been investigated during its passage between parallel plates under magnetic effect and apart at height (h), which takes angular rotation in the vertical direction. Surprisingly, the upper plate has been thought of as permeable, whereas the bottom plate extends from the center on both sides. The goal of this investigation was achieved with the use of velocity charts in x and y directional velocities labeled F' and G, respectively. The thermal status of the system has also been studied using thermal dispersal maps. Skin resistance parameter (C_f) and Nusselt number (Nu) were also computed and shown in tables as parameters of interest. $\beta = 0.1$, $\text{Er} = 0.1$, $\gamma = 0.2$, $\delta = 0.1$, $N_r = 0.1$, $\phi_a = \phi_b = 0.05$, $B_1 = 5$, $B_2 = 0.5$, $B_3 = 0.5$, and $S = 1$ are the used values to get the numerical findings. Experiments constantly have been repeated to ensure that the results are consistent. In general, the findings do not differ by more than a modest percentage point (1 or 2%). In

Table 5: Numerical values and errors of $-\theta'(0)$ for the case $\phi = \phi_a = \phi_b = 0$

S	Current at $Y = 0$	Ref. [41] at $Y = 0$	Error	Current at $Y = 1$	Ref. [41] at $Y = 1$	Error
–1	0.496625	0.496625	3.20×10^{-6}	1.426231	1.426231	2.12×10^{-6}
0	1.000000	1.000000	1.04×10^{-6}	1.000000	1.000000	2.33×10^{-6}
1	1.720366	1.720366	2.01×10^{-6}	0.631314	0.631314	1.22×10^{-6}

addition, the related several data have been checked regularly. We separated the data into two portions once it was gathered. The initial set of data has been used to build a mathematical model that connects the input and goal data. The second set of data was used to validate models, and we were able to get results that were close to the goal and accurate.

6.1 Raman spectra of $[Na\text{-}Alg/MoS_2]^m$ and $[Na\text{-}Alg/MoS_2 + GO]^h$

Figure 6(a) and (b) show Raman spectra and considered $[Na\text{-}Alg/MoS_2]^m$ and $[Na\text{-}Alg/MoS_2 + GO]^h$ thin films. Carboxylate groups are responsible for the inclination of the sodium alginate functional groups to build complex structures with $[MoS_2]^{NPs}$ [42]. From Figure 6(a), the Raman spectra of $[Na\text{-}Alg/MoS_2]^m$ film demonstrated the absorption band in 4,000–3,700 cm^{-1} area because of the stretching vibration band of ν(OH) group. Two strong absorption bands that appear at the range of 3,000–2,600 cm^{-1} can be attributed to stretching ν(–CH) [43]. Noted strips at 1,460 cm^{-1} and 1,415 cm^{-1} were assigned to two types of shrinking vibrations (asymmetric and symmetric) of ν(COO–), correspondingly, and are detailed to the ionic bonding. The cross-linkage of the $[MoS^2]^{NPs}$ with the sodium alginate emerges at the shoulder of 1,150 cm^{-1} for the stretching of both ν(C–C) and ν(C–O) [44]. Stretch band ν(C–C) (1,070 cm^{-1}) shows a lower strength, indicating a greater O–H binding vibration or strongly binding $[MoS_2]^{NPs}$ to sodium alginate guluronic acids which appeared at wave number 1,070 cm^{-1} [45]. Furthermore, guluronic and mannuronic acids are linked to stretching vibration strips analyzed at 890 cm^{-1} as well

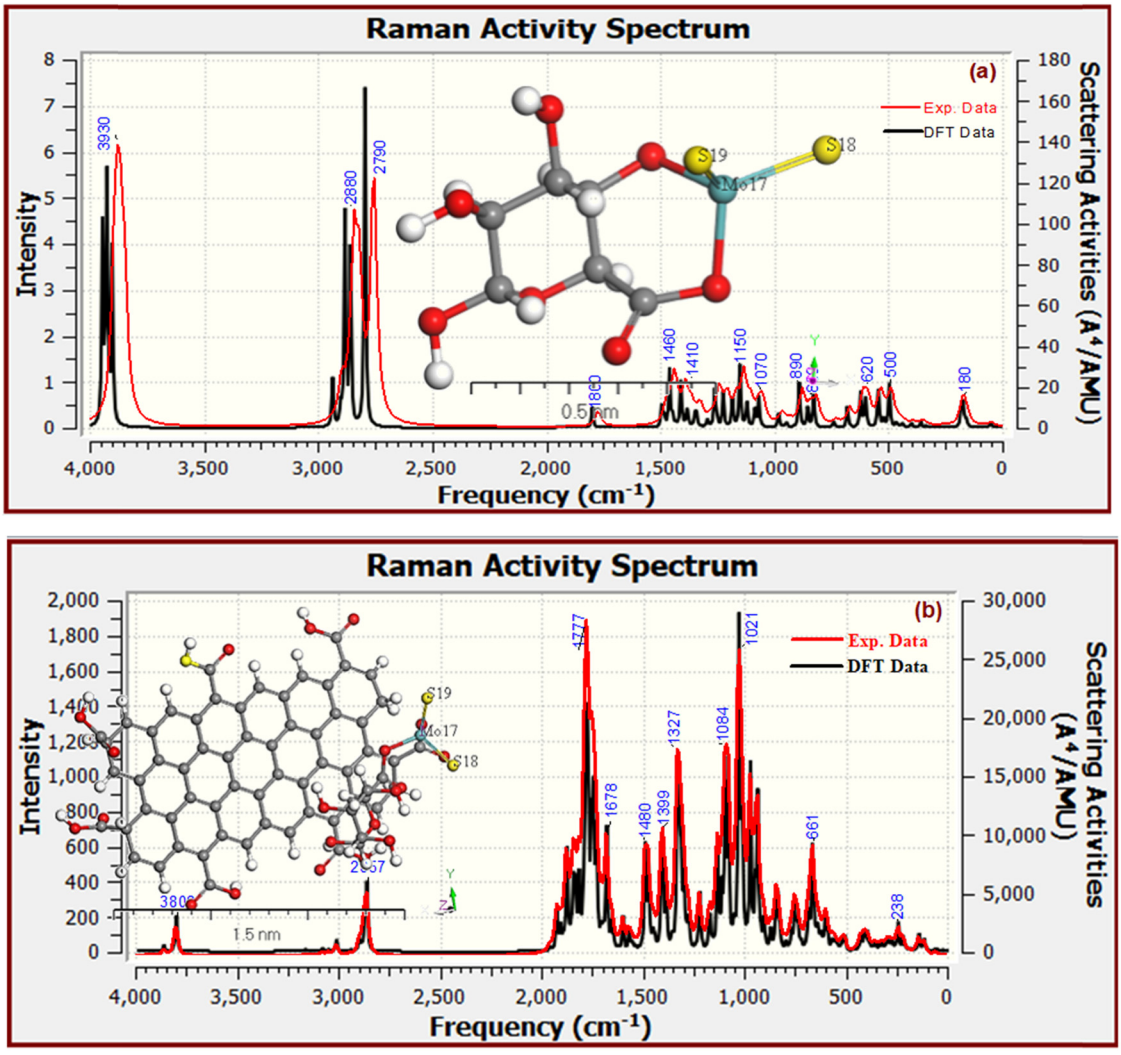

Figure 6: Collective modeled and experimentation IR spectra of (a) $[Na\text{-}Alg/MoS_2]^m$ and (b) $[Na\text{-}Alg/MoS_2 + GO]^h$ nanofluids.

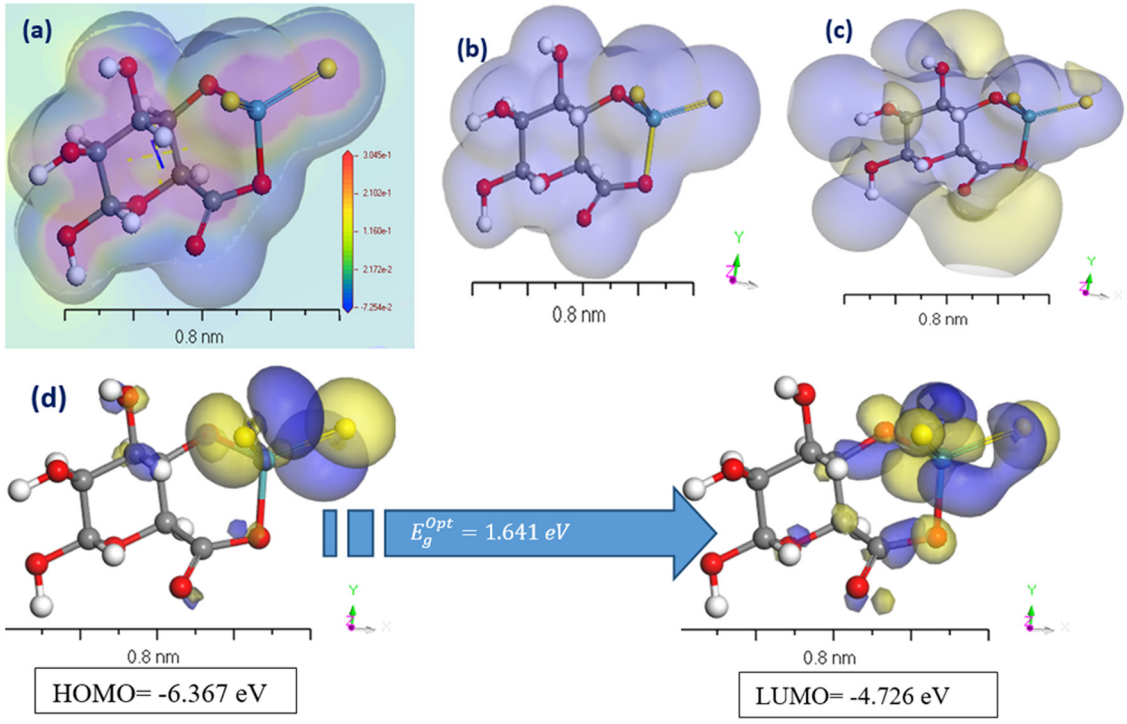

Figure 7: (a) MEP, (b) ED, (c) [P], and (d) HOMO and LUMO computations of [Na-Alg/MoS_2]^m.

as 830 cm^{-1}. Ionic bundling of [MoS^2]^{NPs} and sodium alginate chains has been inferred to be due to minor changes in the carboxyl groups [46]. The intermediate bands at 620 and 500 cm^{-1} in the downfield area are featured to (–O–MoS_2–O–) that described the reaction of MoS_2 with Na-Alg. As shown in spectra Figure 6(b), the strong absorption bands appearing at the range of 2,000–1,600 cm^{-1} wavenumber values for [Na-Alg/MoS_2 + GO]^h thin film can be attributed to the in-plane sp^2 domains of [GO]^{NPs} [47]. The 2D band at 1,777 and 1,678 cm^{-1} is related to ν_{Sym} and ν_{Unsym} (COO–) in GO structure matrix, respectively. The band at 661 cm^{-1} in the downfield area is attributed to the reaction of MoS_2 with Na-Alg and [GO]^{NPs} to form an ionic binding ((Na-Alg)–O–MoS_2–O–(GO)) [48].

The simulated Raman spectra were estimated of [Na-Alg/MoS_2]^m and [Na-Alg/MoS_2 + GO]^h isolated gaseous state. Minor variants among frequencies projected and calculated are seen in Figure 6(a) and (b). Since vibrational types of examined ligands are helpful in achieving minimal symmetry and torque, along with other modes about the plane, it is hard to point out because ring modes degrade, other than imitating. However, the obtained graph shows some clear motions [49]. Obtained experimental ($\lambda_{Exp.}$) and computed ($\lambda_{Cal.}$) data are demonstrated by the subsequent formula for [Na-Alg/MoS_2]^m nanocomposite: $\lambda_{Cal.}$= $0.945\lambda_{Exp.}$ + 17.23 with correlation coefficient (R^2 = 0.989). For [Na-Alg/MoS_2 + GO]^h: $\lambda_{Cal.}$ = $0.981\lambda_{Exp.}$ + 19.27 with correlated factors (R^2 = 0.988).

6.2 Geometric study

Several data have been assessed and implemented of the positive and negative surface ratio effects in electron levels before modeling isolated molecules for [Na-Alg/MoS_2]^m and [Na-Alg/MoS_2 + GO]^h nano-fluid. The results demonstrate that positive surface density is maintained until it reaches the nuclear components; however, the number of negative components decreases with Gaussian 09w/DFT [50]. While the proportion of positive areas is around 68% of the total at 0.002 au, at 0.01 au, the ratio is over 85%. Figures 7(a) and 8(a) indicate that the visual representations of the MEP iso area value of −15 kcal mol^{-1} may be utilized in nanofluid pairs of fields. The $3D_{min}$ principles of $MEP_{V\,max}$ are -7.254×10^{-2} and -1.460×10^{-1} kcal mol^{-1} for [Na-Alg/MoS_2]^m and [Na-Alg/MoS_2 + GO]^h required by MEP's structure, correspondingly. Also, the calculated $MEP_{V\,max}$ and $MEP_{V\,min}$ should take special considerations as predicted based on the presence of alternate electron. The flourishing electron life of its unique pair depends on substituted energy provided by a nanofluid. $MEP_{V\,min}$ is a basic and straightforward technique to determine the pair

power in the solitary pair area. Increasing electron density (ED) in a pair of oxygen atoms is the main feature of the negative $MEP_{V\,min}$ range. Pulling out an electron from the cluster helps minimize the unwanted life of $MEP_{V\,min}$. $MEP_{V\,min}$ concentrated on electrical nanofluid impact estimates that rely on quantities of distinct types to be significantly practical and clearer than structures (OH). In the imagining data of $[Na\text{-}Alg/MoS_2]^m$ and $[Na\text{-}Alg/MoS_2 + GO]^h$, respectively, the nanofluid matrix μ-donating strength is employed. $[Na\text{-}Alg/MoS_2]^m$ and $[Na\text{-}Alg/MoS_2 + GO]^h$ are exchanged for solely the quantity of $MEP_{V\,min}$ when nanofluid movement is not required [51]. Figures 7(b) and 8(b) shows ED for $[Na\text{-}Alg/MoS_2]^m$ and $[Na\text{-}Alg/MoS_2 + GO]^h$, correspondingly. The macrocyclic plane's negative electrostatic potential [P] is symmetrically apparent in all computations [52] and the positive and negative portions vary according to a base group. The sources (DNP) are enlarged in DN to include irrelevant additional extensions with the base folder (4.4), SCF-lenience (0.0001), and maximum SCF-rooms (0.5–102), and multi-polar octupole, as shown in Figures 7(c) and 8(c).

In Figures 7(d) and 8(d), HOMO as well as LUMO are specifications in common reactive descriptors utilizing quantum estimations [53]. Molecular balance can be defined by energy differences among FMOs. This has a vital role in measuring electrical conductivity which is further helpful for understanding electrical transport. Negative E_H and E_L show the stability of the structural matrix. Observed FMOs provide estimations about electrophilic positions inside aromatic compounds. Increment in E_H was obtained with the utilization of An enhancement in E_H was achieved by using the Gutmannat variable approach on M-L sites via M-L augmentation while reducing the length of the strip [54]. The difference in the energy strip explains the relation of load transfer in a molecule. E_g^{Opt} was stated as chemically reactive as well as having kinetic stability. Softness and hardness are included in the stability and reactivity assessment. The greatest value of molecular orbital coefficients decides the location. The appearance of nucleophilic attack on H–O (2), $-CH_2O$ (7), O–H (4), and $-CH_2O$ (10) atoms is HOMO position. E_g^{Opt} are 1.641 and 0.158 eV which are shown in Figures 7(d) and 8(d) for $[Na\text{-}Alg/MoS_2]^m$ and $[Na\text{-}Alg/MoS_2 + GO]^h$, respectively. The E_g^{Opt} for $[Na\text{-}Alg/MoS_2 + GO]^h$ is lesser than E_g^{Opt} for $[Na\text{-}Alg/MoS_2]^m$ because of its soft-ability as well as being more polarizable. Because electrons can have an acceptor, soft particles are deemed responsive rather than hard particles. As the device uses an electrical external charge, it anticipates energy stability. The quentities of HOMO (E_H), LUMO (E_L), E_g^{Opt}, chemical potential (ς), electrophilicity-index (ω), softness (ϑ), electronegativity (χ), hardness (ϵ), ΔNmax, and ϱ are counted in Table 6.

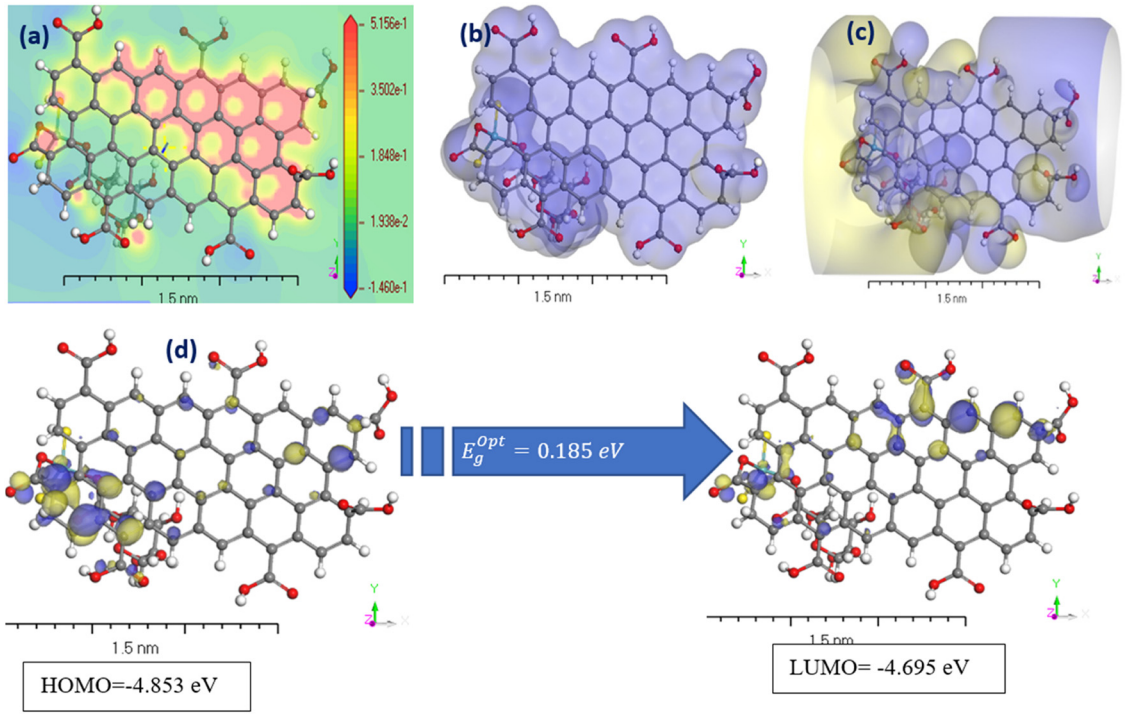

Figure 8: (a) MEP, (b) ED, (c) [P], and (d) HOMO and LUMO computations of $[Na\text{-}Alg/MoS_2 + GO]^h$.

Table 6: Geometry factors/computed DFT for $[Na\text{-}Alg/MoS_2]^m$ and $[Na\text{-}Alg/MoS_2 + GO]^h$

Compound	E_H	E_L	$E_H - E_L$	χ	ς	ϵ	ϑ	ω	ΔN_{max}	ϱ
$[Na\text{-}Alg/MoS_2]^m$	−6.367	−4.726	1.641	5.547	−5.55	−0.821	−0.609	−18.747	−6.76	−1.219
$[Na\text{-}Alg/MoS_2 + GO]^h$	−4.853	−4.695	0.158	4.774	−4.77	−0.079	−6.329	−144.25	−60.43	−12.66

6.3 Consequence of Casson constraint (β)

Flow behaviour affected by Casson constraint (β) on any direction of "x" as well as "y" were described in terms of F' and G in Figure 9(a) and (b), respectively. β is a flow-influencing parameter, which can manipulate viscous conditions by exerting them. An increment in Casson resister (β) hinders fluidity of passing fluid which is seen in every direction. In horizontal conditions of flow, $[Na\text{-}Alg/MoS_2]^m$ nanofluid moves slower than $[Na\text{-}Alg/MoS_2 + GO]^h$. However, in the flow of "y"-direction, NPs experience more added resistance of gravity inclusive of other significance, which leads $[Na\text{-}Alg/MoS_2 + GO]^h$ to slow down more than $[Na\text{-}Alg/MoS_2]^m$. The presence of NPs fills the inter-molecular spaces of the fluid used, leading to this observed behavior. This means that the interfacial distances between the fluid molecules are filled with NPs that have been added, which makes us see that behavior occurring in the case of increasing the Casson constraint in the direction of the vertical axis, especially.

6.4 Outcomes regarding heat generation/absorption constraint (δ)

This parameter is one of the parameters that thermally affects on the heat transference during the fluid flow environment. δ helps in manipulating thermal constraints as

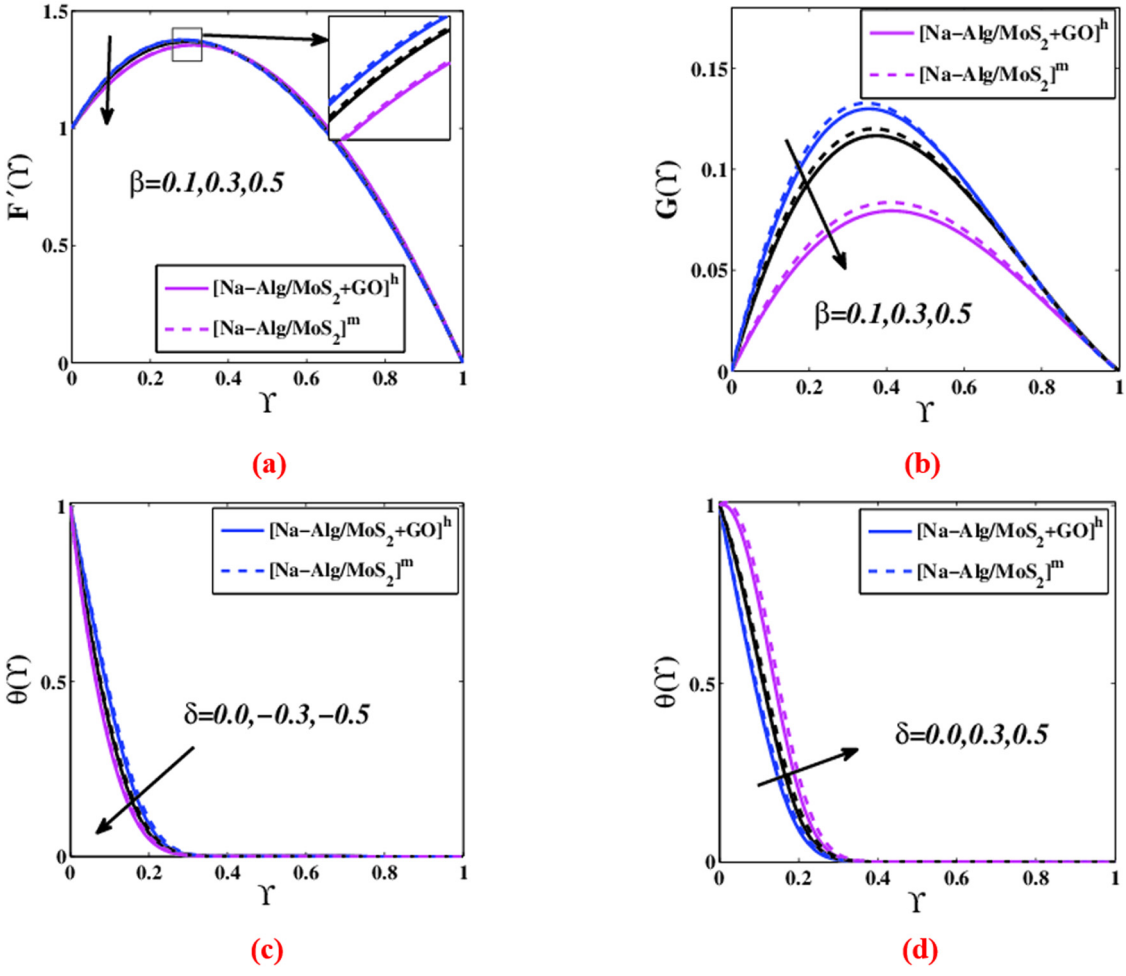

Figure 9: Impact of β on (a) $F'(Y)$ and (b) $G(Y)$. Impact of δ on (c) $\theta(Y)$ and (d) $\theta(Y)$.

($\delta < 0$) is sink and ($\delta > 0$) is generation. Figure 9(c) and (d) disclosed that thermal constraint and thermal dispersion have raise for a heat source and reduced for the heat sink. The heat source raises the rate of potential energy within the system, which causes a temperature rise, on the contrary, in the case of the heat sink. The presence of the heat source affects the molecules in the fluid and stimulates them by increasing the stored internal energy, which greatly increases the collisions between them, which leads to an increase in the temperature of the nanofluid.

6.5 Outcomes regarding local inertia (Er) and porosity (γ) constraints

Figure 10(a) and (b) represent the flow conditions for hiking values of the local inertia parameter (Er). In both displays, it can be noted that the flow gets slower for a certain range due to the force, then later it gets hiked. As a result of increasing the local inertia parameter, it physically slows the movement of molecules inside the nanofluid, and thus the fluid flow velocity decreases and its resistance increases. Porosity γ creates a notable impact on flow behaviors in any flowing situation. Figure 10(c) and (d) showcase such claims, that porosity can pull back the fluidity of both ($[\text{Na-Alg/MoS}_2]^{\text{m}}$) and ($[\text{Na-Alg/MoS}_2 + \text{GO}]^{\text{h}}$) in lateral and vertical directions. Flow velocity is not strongly dependent on porosity for porosities bigger than the critical porosity. For values below the critical porosity, velocity is strongly impacted by porosity, and a little reduction in porosity results in a large increase in velocity.

6.6 Consequence of fractional volume of nano (ϕ_{nf}) and hybrid (ϕ_{hbnf}) nanofluids

Dominance of efficiency of mono and HNFs was influenced by the NPs proportion in the fluid levels. Fractional volume rate

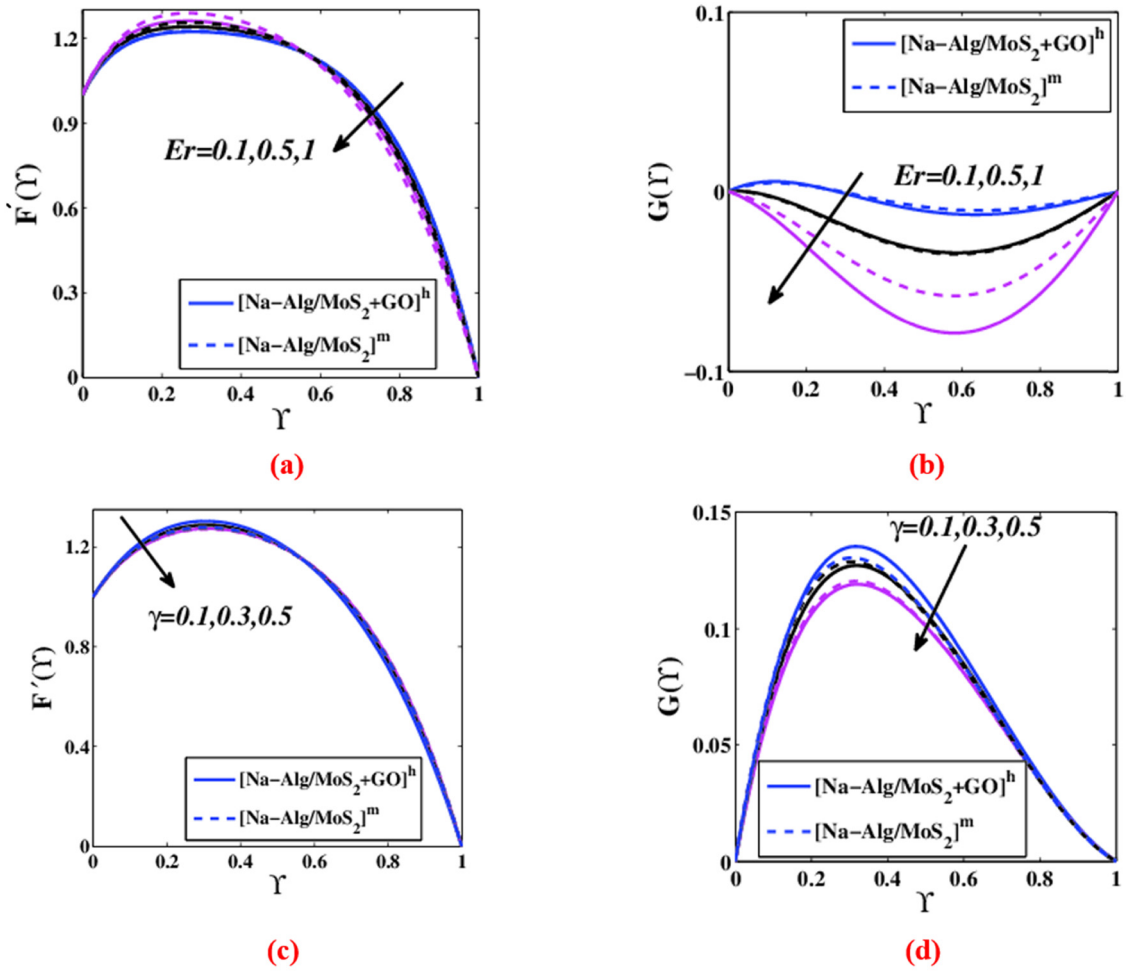

Figure 10: Impact of Er on (a) $F'(Y)$and (b) $G(\eta)$. Impact of γ on (c) $F'(Y)$ and (d) $G(\eta)$.

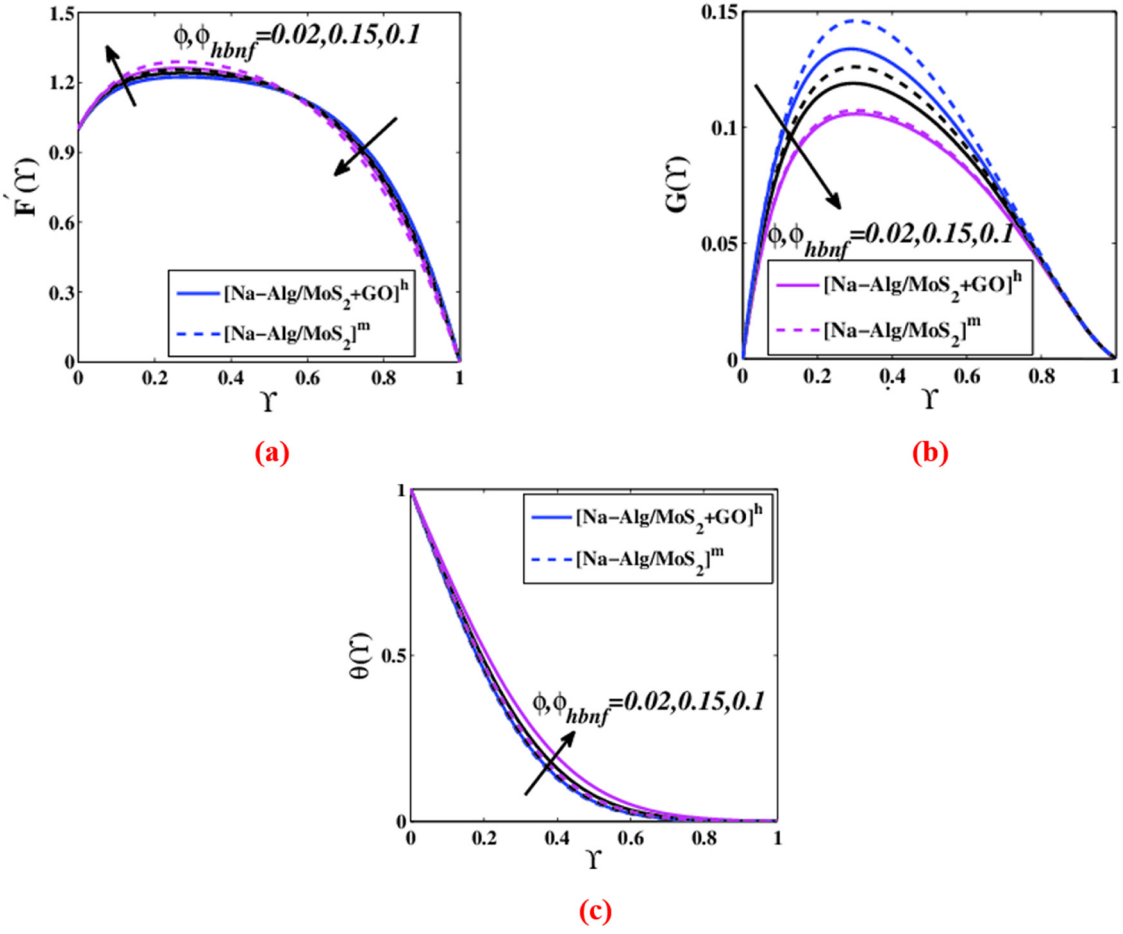

Figure 11: Changes in (a) $F'(Y)$, (b) $G(Y)$, and (c) $\theta(Y)$ with ϕ and ϕ_{hbnf}.

resists the flow speed which can be observed in Figure 11(a) and (b), respectively, in lateral and vertical flow directions. Figure 11(c) shows the thermal dispersion in interested surrounding for cumulative values of a fractional volume of both mono ϕ_{nf} and hybrid ϕ_{hbnf}. Because the NPs were designed for heat transmission, they must push and capture heat from the surface, reflecting an increase in the thermal state. Increasing the concentration of NPs inside the fluid reduces the movement resistance of the fluid flow as a result of reducing the interlayer distances between the molecules that are filled with NPs, and thus the stored thermal energy increases, which raises the temperature of the nanofluid.

6.7 Outcomes about Reynolds number (B_1)

Variations in Reynolds number B_1 could directly affect the fluidity in the system and eventually, could influence the thermal constraints. Figure 12 clarifies the abovementioned assertions to be right. Interestingly, improvement in Reynolds number B_1 results in increasing the lateral velocity F', while pulling down the vertical velocity G of [Na-Alg/MoS_2 + GO]$^{\text{h}}$ and [Na-Alg/MoS_2]$^{\text{m}}$. This might be owing to the magnetic and gravitational parts of vertical fluidity being supported, as seen in Figure 12(a) and (b). Figure 12(c) represents the dwindling thermal dispersal for the Reynolds number B_1, which swifts fluids due to the lack of time to grasp temperature from the sheet. The physical reason for this is that the Reynolds number is inversely proportional to the viscosity of the fluid, which creates the effects seen on the flow velocity and temperature of the nanofluid.

6.8 Outcomes about rotation constraint (B_2)

Unlike the flow and thermal behaviors of Reynolds number B_1, Figure S1 shows the current behaviour of the rotation constraint B_2 in contrast to the adjacent speed along with thermal dispersion and helps oblique speed of

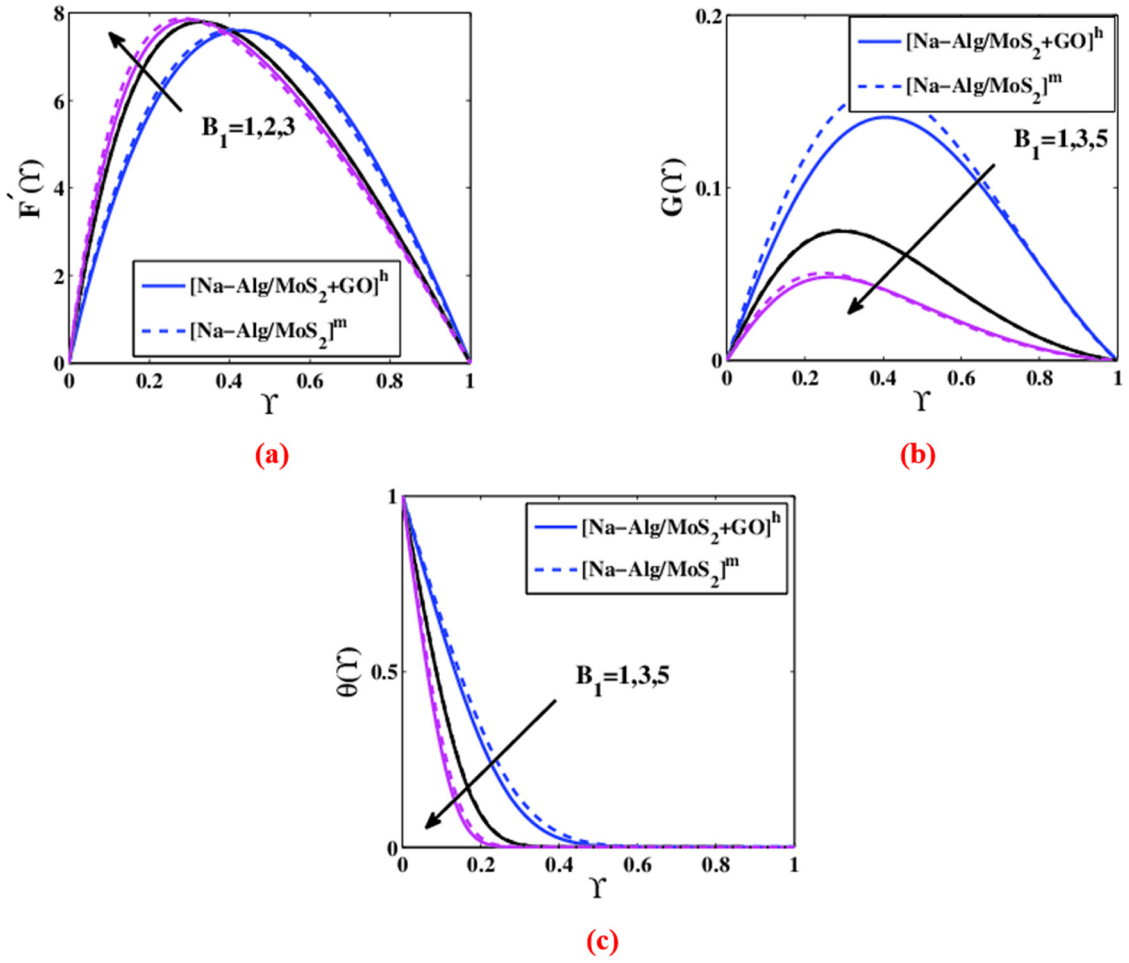

Figure 12: Changes in (a) $F'(Y)$, (b) $G(Y)$, and (c) $\theta(Y)$ with parameter B_1.

$[\text{Na-Alg/MoS}_2 + \text{GO}]^{\text{h}}$ and $[\text{Na-Alg/MoS}_2]^{\text{m}}$ for its increment. As revolving impact reduces lateral flow, it increases transverse fluidity and enhances particle mobility in the fluids, allowing them to absorb more heat and thereby increasing thermal diffusion in the system. Since $B = (\Omega h^2)/\nu_{\text{f}}$, then the rotation parameter is inversely proportional to the viscosity of the fluid. This makes, from a physical point of view, its effect like that of the Reynolds number.

6.9 Consequence of Hartman number

Hartman number B_3 shows the strength of magnetic interaction which was applied in transverse direction to the sheets. As it opposes lateral velocity F', it helps "y" directional fluidity by both fluids. Lorentz force acts favorably for the thermal transference of $[\text{Na-Alg/MoS}_2 + \text{GO}]^{\text{h}}$ and $[\text{Na-Alg/MoS}_2]^{\text{m}}$, all these interactions can be viewed through Figure S2(a–c). Aggregated values regarding Hartman number B_3 resulted in the thermal boundary layer being broader. From Figure S2(d), it is evidence that for increasing values of radiation parameter, the thermal distribution is increased too. The physical reason for this can be traced back to the fact that the Lorenz force is the one that forms this effect and strongly works to cause this on both the horizontal and vertical speed as well as the temperature.

6.10 Nusselt number in the downstairs surface

The parametrical studies have been conducted for factors like Reynolds number B_1, rotational factor B_2, and Hartman number B_3 at a lower wall ($Y = 0$) on heat transference rate of $[\text{Na-Alg/MoS}_2 + \text{GO}]^{\text{h}}$. Figure S3(a)–(c) show these efforts, while the Reynolds number B_1 supports the

Table 7: Variation in skin friction coefficients

ϕ	[Na-Alg/MoS_2]^m		[Na-Alg/MoS_2 + GO]^h	
	$\sqrt{Re_x}C_f$ at $Y = 0$	$\sqrt{Re_x}C_f$ at $Y = 1$	$\sqrt{Re_x}C_f$ at $Y = 0$	$\sqrt{Re_x}C_f$ at $Y = 1$
0.005	2.87602	6.86684	2.26787	5.50274
0.03	2.84188	6.39679	2.32069	5.56099
0.05	2.77929	6.87684	2.32410	5.55447
0.08	2.67667	7.48695	2.33401	5.57782
0.1	2.62686	7.77967	2.31331	5.58481

Table 8: Variation in local Nusselt numbers

ϕ	[Na-Alg/MoS_2]^m		[Na-Alg/MoS_2 + GO]^h		Relative% at $Y = 0$
	$\frac{Nu_x}{\sqrt{Re_x}}$ at $Y = 0$	$\frac{Nu_x}{\sqrt{Re_x}}$ at $Y = 1$	$\frac{Nu_x}{\sqrt{Re_x}}$ at $Y = 0$	$\frac{Nu_x}{\sqrt{Re_x}}$ at $Y = 1$	$\frac{Nu_{(MoS_2-GO)}-Nu_{(MoS_2)}}{Nu_{(MoS_2-GO)}}$ ×100
0.01	1.56655	0.69595	1.66623	0.65307	6.16683
0.02	1.48430	0.73336	1.65562	0.65753	10.9124
0.03	1.42083	0.76356	1.64510	0.66197	14.6298
0.04	1.37045	0.78840	1.63468	0.66639	17.5853
0.05	1.32955	0.80918	1.62435	0.67077	19.9601
0.06	1.29573	0.82679	1.61411	0.67514	21.883

local thermal transference rate, the other two constraints such as the rotating constraint B_2 and Hartman number B_3 gets reduced.

6.11 Nusselt number in an upstairs surface

Figure S4(a)–(c) depict the parametrical analyses same as above but in the upper wall ($Y = 1$) for the Reynolds number B_1, rotational factor B_2, as well as the Hartmann number B_3. Both Reynolds number B_1 and rotating constraint B_2 were behaved unchanged in the upper wall too. Hartman number B_3 changes in porosity were acts in favor of the thermal transferring rate employing the local Nusselt number.

6.12 Fluid level transference rate

Exclusive bar grids were comparatively plotted on suction for both [Na-Alg/MoS_2 + GO]^h and [Na-Alg/MoS_2 + GO]^h nanofluids given the directional aspects. Figure S5 demonstrates that, streamlines is accumulated due to the injection in a closer range than the suction is applied. The characteristics of porous materials are affected by pore shape, pore strut/wall size and form, surface coarseness, and surface space, in addition to penetrability and pore size.

6.13 Variation in skin resistance factors

Though the main attention was on fluid thermal performance, the frictional surface is to be estimated for additional effects on thermal properties and it can be viewed in Table 7. Two different physical areas having lower and upper sheets were used for it. The skin's resistance to both fluids increases more in the upper wall than it does in the sheet located below. The skin resistance of HNF is much lower than that of nanofluid. The increase was attained in mono nanofluid under circumstances of fractional volume for higher quantities of ϕ. The parameter of drag force about nanofluid decreases when it is at a lower wall, but HNF increases when it is in other circumstances.

6.14 Changes in local Nusselt quantities

Rate of local thermal transference about [Na-Alg/MoS_2 + GO]^h and [Na-Alg/MoS_2]^m are exhibited in Table 8 for fractional volume (ϕ). It is clear that a better rate of thermal transfer may be attained in the upper wall rather than the lower wall. Around 6.2–21.9% thermal transfer has been obtained.

7 Conclusion

Theoretical simulation and experimental inspection of the flow and heat transmission analysis of Casson nanofluids of a combination of molybdenum disulfide with sodium alginate in [Na-Alg/MoS_2 + GO]^h flows based on [Na-Alg/MoS_2]^m and GO were investigated inside solar aircraft wings as two parallel surfaces in a PTSC use. Mono [Na-Alg/MoS_2]^m and [Na-Alg/MoS_2 + GO]^h thin films have been formulated by using PVD method. DFT is calculated using the package DFT in *Material Studio 7.0 software*. The simulated analysis based on LUMO, HOMO as well as other active nanofluid variables. The main results are summarized as follows:

- Regarding fluidity in the lateral "x" direction, as a standalone constraint, Reynolds number B_1 assists the flow while all other influencing constraints tend to suppress it.

- Constraints of rotation B_2 and Hartman number B_3 tend to boost the upright fluidity in the "y" direction for both combinations of [Na-Alg/MoS_2 + GO]^h and [Na-Alg/MoS_2]^m. The rest of the constraints act against it.
- Drag force is increased with the increase in the size of nanomolecules, especially in the downstairs wall than the upstairs.
- Upper wall has a higher thermal transference rate than the lower wall. The Hartman number, other than the Reynolds number, had a role in improving the heat transference rate.
- When GO is added, the hybrid combination [Na-Alg/MoS_2 + GO]^h is made, which shows an advance in major heat transfer compared to the mono mixture of [Na-Alg/MoS_2]^m.
- The ratio percentage between energy bandgap E_g^{Opt} values for [Na-Alg/MoS_2]^m and [Na-Alg/MoS_2 + GO]^h decreased by 82.43%, leading to more efficiency of [Na-Alg/MoS_2 + GO]^h as a coolant in the solar energy applications.

There are many constructive studies with valuable ideas that can be worked on in future studies and transform the mathematical system into a system based on hybrid nanofluids so that they can be studied theoretically and experimentally for different fluids and different NPs as well. The important examples of these studies are available in previous literature [55–57]. It can be said that in the near future we are currently working on extending the current concept in this study to include the main ideas of previous literature [58–63].

Acknowledgments: The authors extend their appreciation to the Deanship of Scientific Research at King Khalid University for funding this work through large group Research Project under Grant number RGP2/251/44.

Funding information: This work was funded by the Deanship of Scientific Research at King Khalid University through large group Research Project under Grant number RGP2/251/44.

Author contributions: All authors have accepted responsibility for the entire content of this manuscript and approved its submission.

Conflict of interest: The authors state no conflict of interest.

Data availability statement: All data generated or analyzed during this study are included in this published article [and its supplementary information files].

References

[1] Li Y, Tung S, Schneider E, Xi S. A review on development of nanofluid preparation and characterization. Powder Technol. 2009;196(2):89–101.
[2] Khan M, Lone SA, Rasheed A, Alam MN. Computational simulation of Scott-Blair model to fractional hybrid nanofluid with Darcy medium. Int Commun Heat Mass Transf. 2022;130:105784.
[3] Khan M, Rasheed A. Computational analysis of heat transfer intensification of fractional viscoelastic hybrid nanofluids. Math Prob Eng. 2021;2021:1–24.
[4] Peng XF, Yu XL, Xia LF, Zhong X. Influence factors on suspension stability of nanofluids. J Zhejiang Univ Eng Sci. 2007;41(4):577.
[5] Khan M, Rasheed A. A numerical study of hybrid nanofluids near an irregular 3D surface having slips and exothermic effects. Proc Inst Mech Eng. 2022;236(4):1273–82.
[6] Hwang YJ, Lee JK, Lee CH, Jung YM, Cheong SI, Lee CG, et al. Stability and thermal conductivity characteristics of nanofluids. Thermochim Acta. 2007;455(1–2):70–4.
[7] Wang BX, Li CH, Peng XF. Research on stability of nano-particle suspension. J Univ Shanghai Sci Technol. 2003;25(3):209–12.
[8] Liu DM. Influence of dispersant on powders dispersion and properties of zirconia green compacts. Ceram Int. 2000;26(3):279–87.
[9] Zhu D, Li X, Wang N, Wang X, Gao J, Li H. Dispersion behavior and thermal conductivity characteristics of Al_2O_3–H_2O nanofluids. Curr Appl Phys. 2009;9(1):131–9.
[10] Choi SUS. Nanofluids: A new field of scientific research and innovative applications. Heat Transf Eng. 2008;29(5):429–31.
[11] Sidik NAC, Jamil MM, Japar WMAA, Adamu IM. A review on preparation methods, stability and applications of hybrid nanofluids. Renew Sustain Energy Rev. 2017;80:1112–22.
[12] Choi SU, Eastman JA. Enhancing thermal conductivity of fluids with nanoparticles (No. ANL/MSD/CP-84938; CONF-951135-29). IL (United States): Argonne National Lab; 1995.
[13] Waini I, Ishak A, Pop I. Hybrid nanofluid flow towards a stagnation point on a stretching/shrinking cylinder. Sci Rep. 2020;10(1):1–12.
[14] Shahsavar A, Bahiraei M. Experimental investigation and modeling of thermal conductivity and viscosity for non-Newtonian hybrid nanofluid containing coated CNT/Fe_3O_4 nanoparticles. Powder Technol. 2017;318:441–50.
[15] Bahiraei M, Godini A, Shahsavar A. Thermal and hydraulic characteristics of a minichannel heat exchanger operated with a non-Newtonian hybrid nanofluid. J Taiwan Inst Chem Eng. 2018;84:149–61.
[16] Mustafa M, Bard D, Bhimji W, Lukić Z, Al-Rfou R, Kratochvil JM. CosmoGAN: creating high-fidelity weak lensing convergence maps using Generative Adversarial Networks. Comput Astrophys Cosmol. 2019;6(1):1.
[17] Wang R, Kashinath K, Mustafa M, Albert A, Yu R. Towards physics-informed deep learning for turbulent flow prediction. In: Proceedings of the 26th ACM SIGKDD, International Conference on Knowledge Discovery & Data Mining; 2020. p. 1457–66.
[18] Makanda G, Shaw S, Sibanda P. Effects of radiation on MHD free convection of a Casson fluid from a horizontal circular cylinder with partial slip in non-Darcy porous medium with viscous dissipation. Bound Value Probl. 2015;2015(1):1–14.

[19] Hayat S, Hayat Q, Alyemeni MN, Wani AS, Pichtel J, Ahmad A. Role of proline under changing environments: a review. Plant Signal Behav. 2012;7(11):1456–66.
[20] Mukhopadhyay M. Total quality management in education. SAGE Publications Pvt. Limited; 2020.
[21] Rajan G, Raju R, Jinachandran S, Farrar P, Xi J, Prusty BG. Polymerisation shrinkage profiling of dental composites using optical fibre sensing and their correlation with degree of conversion and curing rate. Sci Rep. 2019;9(1):1–10.
[22] Timofeev VN, Khatsayuk MY. Theoretical design fundamentals for MHD stirrers for molten metals. Magnetohydrodynamics. 2016;52(4):495–506.
[23] Raptis A, Perdikis C, Takhar HS. Effect of thermal radiation on MHD flow. Appl Math Comput. 2004;153(3):645–9.
[24] Trouwborst ML, Van Der Molen SJ, Van, Wees BJ. The role of Joule heating in the formation of nanogaps by electromigration. J Appl Phys. 2006;99(11):114316.
[25] Huang D, Wu Z, Sunden B. Effects of hybrid nanofluid mixture in plate heat exchangers. Exp Therm Fluid Sci. 2016;72:190–6.
[26] Lakew AA, Bolland O. Working fluids for low-temperature heat source. Appl Therm Eng. 2010;30(10):1262–8.
[27] Wang J, Zabaras N. Using Bayesian statistics in the estimation of heat source in radiation. Int J Heat Mass Transf. 2005;48(1):15–29.
[28] Fujii T. Theory of the steady laminar natural convection above a horizontal line heat source and a point heat source. Int J Heat Mass Transf. 1963;6(7):597–606.
[29] Suresh S, Venkitaraj KP, Selvakumar P, Chandrasekar M. Effect of Al_2O_3–Cu/water hybrid nanofluid in heat transfer. Exp Therm Fluid Sci. 2012;38:54–60.
[30] Shomalian K, Bagheri-Mohagheghi M-M, Ardyanian M. Synthesis and characterization of porous nanoparticles of molybdenum sulfide (MoS_2) chalcogenide semiconductor prepared by polymerizing-complexing sol–gel method. J Mater Sci: Mater Electron. 2017;28:14331–40.
[31] Eid MR, Al-Hossainy AF. High-performance nanofluid synthesis and DFT-TDDFT study of graphene nanosheets along bent surface for enhanced oil-recovery implementations. Case Stud Therm Eng. 2021;25:100983.
[32] Al-Hossainy AF, Eid MR. Combined experimental thin films, TDDFT-DFT theoretical method, and spin effect on $[PEG\text{-}H_2O/ZrO_2 + MgO]^h$ hybrid nanofluid flow with higher chemical rate. Surf Interfaces. 2021;23:100971.
[33] Abd-Elmageed A, Ibrahim S, Bourezgui A, Al-Hossainy A. Synthesis, DFT studies, fabrication, and optical characterization of the $[ZnCMC]^{TF}$ polymer (organic/inorganic) as an optoelectronic device. New J Chem. 2020;44:8621–37.
[34] Becke AD. Density-functional thermochemistry. I. The effect of the exchange-only gradient correction. J Chem Phys. 1992;96:2155–60.
[35] Lee C, Yang W, Parr RG. Development of the Colle-Salvetti correlation-energy formula into a functional of the electron density. Phys Rev B. 1988;37:785.
[36] Frisch M, Trucks G, Schlegel HB, Scuseria GE, Robb MA, Cheeseman JR, et al. Gaussian 09, Revisiond. 01. 200, Wallingford CT: Gaussian, Inc: 2019.
[37] Khan A, Saeed A, Gul T, Mukhtar S, Ali I, Jawad M. Radiative swirl motion of hydromagnetic Casson nanofluid flow over rotary cylinder using Joule dissipation impact. Phys Scr. 2021;96(4):045206.
[38] Jamshed W, Nasir NAM, Isa SM, Safdar R, Shahzad F, Nisar KS, et al. Thermal growth in solar water pump using Prandtl–Eyring hybrid nanofluid: a solar energy application. Sci Rep. 2021;11(1):18704.
[39] Cebeci T, Bradshaw P. Physical and Computational Aspects of Convective Heat Transfer. New York: Springer; 1988.
[40] Keller HB. Numerical Methods for Two-Point. Boundary Value Problems. New York: Dover Publications; 1992.
[41] Hussain ST, Haq RU, Khan ZH, Nadeem S. Water driven flow of carbon nanotubes in a rotating channel. J Mol Liq. 2016;214:136–44.
[42] Daemi H, Barikani M. Synthesis and characterization of calcium alginate nanoparticles, sodium homopolymannuronate salt and its calcium nanoparticles. Sci Iran. 2012;6:2023–8.
[43] Al-Hossainy AF, Eid MR, Zoromba MS. Structural, DFT, optical dispersion characteristics of novel [DPPA-Zn-MR (Cl)(H_2O)] nanostructured thin films. Mater Chem Phys. 2019;232:180–92.
[44] Fan A, Hu Y, Ma W, Wang H, Zhang X. Dual-wavelength laser flash Raman spectroscopy method for in-situ measurements of the thermal diffusivity: principle and experimental verification. J Therm Sci. 2019;28(2):159–68.
[45] Jayeoye TJ, Rujiralai T. Green, in situ fabrication of silver/poly (3-aminophenyl boronic acid)/sodium alginate nanogel and hydrogen peroxide sensing capacity. Carbohydr Polym. 2020;246:116657.
[46] Pereira R, Carvalho A, Vaz DC, Gil M, Mendes A, Bártolo P. Development of novel alginate based hydrogel films for wound healing applications. Int J Biol Macromol. 2013;52:221–30.
[47] Qiu L, Du Y, Bai Y, Feng Y, Zhang X, Wu J, et al. Experimental characterization and model verification of thermal conductivity from mesoporous to macroporous SiOC ceramics. J Therm Sci. 2021;30(2):465–76.
[48] Ibrahim A, Al-Hossainy A. Thickness dependence of structural and optical properties of novel 2-((1, 1-bis (diphenylphosphino)-2-phenylpropan-2-yl)-chromium tetracarbonyl-amino)-3-phenylpropanoic acid copper (II)(DPP-Cr-Palan-Cu) nanocrystalline thin film. Synth Metals. 2015;209:389–98.
[49] Al-Hossainy A, Ibrahim A, Mogharbel RT, Ibrahim SM. Synthesis of novel keto-bromothymol blue in different media using oxidation–reduction reactions: combined experimental and DFT-TDDFT computational studies. Chem Pap. 2021;75:3103–18.
[50] Abdel-Aziz M, Al-Hossainy A, Ibrahim A, Abd El-Maksoud S, Zoromba MS, Bassyouni M, et al. Synthesis, characterization and optical properties of multi-walled carbon nanotubes/aniline-o-anthranilic acid copolymer nanocomposite thin films. J Mater Sci: Mater Electron. 2018;29:16702–14.
[51] Zinatloo-Ajabshir S, Salavati-Niasari M. Facile route to synthesize zirconium dioxide (SiO_2) nanostructures: structural, optical and photocatalytic studies. J Mol Liq. 2016;216:545–51.
[52] Majedi A, Abbasi A, Davar F. Green synthesis of zirconia nanoparticles using the modified Pechini method and characterization of its optical and electrical properties. J Sol-Gel Sci Technol. 2016;77:542–52.
[53] Zoromba MS, Abdel-Aziz M, Bassyouni M, Attar A, Al-Hossainy A. Synthesis and characterization of Poly (ortho-aminophenol-co-para-toluidine) and its application as semiconductor thin film. J Mol Struct. 2021;1225:129131.
[54] Liu L, Miao L, Li L, Li F, Lu Y, Shang Z, et al. Molecular electrostatic potential: a new tool to predict the lithiation process of organic battery materials. J Phys Chem Lett. 2018;9:3573–9.
[55] Khan M, Rasheed A. Scott-Blair model with unequal diffusivities of chemical species through a Forchheimer medium. J Mol Liq. 2021;341:117351.
[56] Khan M, Rasheed A, Salahuddin T, Ali S. Chemically reactive flow of hyperbolic tangent fluid flow having thermal radiation and double

stratification embedded in porous medium. Ain Shams Eng J. 2021;12(3):3209–16.
[57] Khan M, Rasheed A. Numerical implementation and error analysis of nonlinear coupled fractional viscoelastic fluid model with variable heat flux. Ain Shams Eng J. 2022;13(3):101614.
[58] Ali FH, Hamzah HK, Hussein AK, Jabbar MY, Talebizadehsardari P. MHD mixed convection due to a rotating circular cylinder in a trapezoidal enclosure filled with a nanofluid saturated with a porous media. Int J Mech Sci. 2020;181:105688.
[59] Li Z, Hussein AK, Younis O, Rostami S, He W. Effect of alumina nanopowder on the natural convection of water under the influence of a magnetic field in a cavity and optimization using RMS: Using empirical correlations for the thermal conductivity and a sensitivity analysis. Int Commun Heat Mass Transf. 2020;112:104497.
[60] Li Z, Hussein AK, Younis O, Afrand M, Feng S. Natural convection and entropy generation of a nanofluid around a circular baffle inside an inclined square cavity under thermal radiation and magnetic field effects. Int Commun Heat Mass Transf. 2020;116:104650.
[61] Ali B, Hussain S, Nie Y, Hussein AK, Habib D. Finite element investigation of Dufour and Soret impacts on MHD rotating flow of Oldroyd-B nanofluid over a stretching sheet with double diffusion Cattaneo–Christov heat flux model. Powder Technol. 2021;377:439–52.
[62] Biswal U, Chakraverty S, Ojha BK, Hussein AK. Numerical investigation on nanofluid flow between two inclined stretchable walls by optimal homotopy analysis method. J Comput Sci. 2022;63:101759.
[63] Ali B, Khan SA, Hussein AK, Thumma T, Hussain S. Hybrid nanofluids: Significance of gravity modulation, heat source/sink, and magnetohydrodynamic on dynamics of micropolar fluid over an inclined surface via finite element simulation. Appl Math Comput. 2022;419:126878.